

1 On the drivers of droplet variability in Alpine mixed-phase 2 clouds

3
4 Paraskevi Georgakaki¹, Aikaterini Bougiatioti², Jörg Wieder³, Claudia Mignani⁴, Fabiola
5 Ramelli³, Zamin A. Kanji³, Jan Henneberger³, Maxime Hervo⁵, Alexis Berne⁶, Ulrike
6 Lohmann³ and Athanasios Nenes^{1,7}

7 ¹Laboratory of Atmospheric Processes and their Impacts, School of Architecture, Civil & Environmental
8 Engineering, École Polytechnique Fédérale de Lausanne, Lausanne, CH-1015, Switzerland

9 ²Institute for Environmental Research & Sustainable Development, National Observatory of Athens, P. Penteli,
10 GR-15236, Greece

11 ³Department of Environmental Systems Science, Institute for Atmospheric and Climate Science, ETH Zurich,
12 Zurich, CH-8092, Switzerland

13 ⁴Department of Environmental Sciences, University of Basel, Basel, CH-4056, Switzerland

14 ⁵Federal Office of Meteorology and Climatology, MeteoSwiss, Payerne, CH-1530, Switzerland

15 ⁶Environmental Remote Sensing Laboratory, School of Architecture, Civil & Environmental Engineering, École
16 Polytechnique Fédérale de Lausanne, Lausanne, CH-1015, Switzerland

17 ⁷Center for Studies of Air Quality and Climate Change, Institute of Chemical Engineering Sciences, Foundation
18 for Research and Technology Hellas, Patras, GR-26504, Greece

19 *Correspondence to:* Athanasios Nenes (athanasios.nenes@epfl.ch).
20

21 **Abstract**

22 Droplet formation provides a direct microphysical link between aerosols and clouds (liquid or
23 mixed-phase), and its adequate description poses a major challenge for any atmospheric model.
24 Observations are critical for evaluating and constraining the process. Towards this, aerosol size
25 distributions, cloud condensation nuclei, hygroscopicity and lidar-derived vertical velocities
26 were observed in Alpine mixed-phase clouds during the Role of Aerosols and Clouds Enhanced
27 by Topography on Snow (RACLETS) field campaign in the Davos, Switzerland region during
28 February and March 2019. Data from the mountain-top site of Weissfluhjoch (WFJ) and the
29 valley site of Davos Wolfgang are studied. These observations are coupled with a state-of-the
30 art droplet activation parameterization to investigate the aerosol-cloud droplet link in mixed-
31 phase clouds. The mean CCN-derived hygroscopicity parameter, κ , at WFJ ranges between
32 0.2-0.3, consistent with expectations for continental aerosol. κ tends to decrease with size,
33 possibly from an enrichment in organic material associated with the vertical transport of fresh
34 ultrafine particle emissions (likely from biomass burning) from the valley floor in Davos. The
35 parameterization provides droplet number that agrees with observations to within ~25%. We
36 also find that the susceptibility of droplet formation to aerosol concentration and vertical
37 velocity variations can be appropriately described as a function of the standard deviation of the
38 distribution of updraft velocities, σ_w , as the droplet number never exceeds a characteristic limit,
39 termed “limiting droplet number”, of $\sim 150\text{-}550\text{ cm}^{-3}$, which depends solely on σ_w . We also
40 show that high aerosol levels in the valley, most likely from anthropogenic activities, increase

41 cloud droplet number, reduce cloud supersaturation ($< 0.1\%$) and shift the clouds to a state that
42 is less susceptible to aerosol and become very sensitive to vertical velocity variations. The
43 transition from aerosol to velocity-limited regime depends on the ratio of cloud droplet number
44 to the limiting droplet number, as droplet formation becomes velocity-limited when this ratio
45 exceeds 0.65. Under such conditions, droplet size tends to be minimal, reducing the likelihood
46 that large drops are present that would otherwise promote glaciation through rime splintering
47 and droplet shattering. Identifying regimes where droplet number variability is dominated by
48 dynamical – rather than aerosol – changes is key for interpreting and constraining when and
49 which types of aerosol effects on clouds are active.

50

51 **1. Introduction**

52 Orographic clouds, and the precipitation they generate, play a major role in Alpine weather and
53 climate (e.g., Roe, 2005; Grubisic and Billings, 2008; Saleeby et al., 2013; Vosper et al., 2013;
54 Lloyd et al., 2015). The formation and evolution of orographic clouds involves a rich set of
55 interactions at different spatial and temporal scales encompassing fluid dynamics, cloud
56 microphysics and orography (Roe, 2005; Rotunno and Houze, 2007). Atmospheric aerosol
57 particles modulate the microphysical characteristics of orographic clouds by serving as cloud
58 condensation nuclei (CCN) that form droplets, or ice nucleating particles (INPs) that form ice
59 crystals (e.g., Pruppacher and Klett, 1997; Muhlbauer and Lohmann, 2009; Zubler et al., 2011;
60 Saleeby et al., 2013).

61 Emissions of aerosol particles acting as CCN and INPs can affect the microphysical and
62 radiative properties of clouds with strong (but highly uncertain) effects on local and regional
63 climate (IPCC, 2013; Seinfeld et al., 2016). Aerosol interactions with orographic clouds are
64 subject to even larger uncertainties, owing in part to the complex flows generated by the
65 interaction of the large-scale flow with the mesoscale orographic lifting and condensation, and
66 complex anisotropic turbulent air motions that arise (Roe, 2005; Smith, 2006; Rotunno and
67 Houze, 2007). Most importantly, orographic clouds are often mixed-phase clouds (MPCs),
68 which are characterized by the simultaneous presence of supercooled liquid water droplets and
69 ice crystals (Lloyd et al., 2015; Farrington et al., 2016; Lohmann et al., 2016; Henneberg et al.,
70 2017). MPCs remain one of the least understood cloud types, due to the multiple and highly
71 nonlinear cloud microphysical pathways that can affect their properties and evolution. MPCs
72 tend to glaciate (i.e., transition to pure ice clouds) over time because of the Bergeron-Findeisen
73 process, which is the rapid growth of ice crystals at the expense of the evaporating cloud

74 droplets, owing to the higher saturation vapor pressure of liquid water over ice (Bergeron,
75 1935; Findeisen, 1938). Aerosol concentrations may also alter the microphysical pathways
76 active in MPCs and ultimately drive their glaciation state. For instance, increase in CCN
77 concentrations leads to more numerous and smaller cloud droplets, reducing the riming
78 efficiency of ice crystals and therefore the hydrometeor crystal mass and the amount of
79 precipitation (Lohmann and Feichter, 2005; Lance et al., 2011; Lohmann, 2017). This
80 mechanism counters the glaciation indirect effect, where increases in INP concentrations
81 elevate ice crystal number concentration (ICNC) and promotes the conversion of liquid water
82 to ice - therefore the amount of ice-phase precipitation (Lohmann, 2002). Increases in CCN
83 can also decrease cloud droplet radius, and impede cloud glaciation, owing to reductions in
84 secondary ice production (SIP), which includes rime splintering, collisional break-up and
85 droplet shattering (Field et al., 2017; Sotiropoulou et al., 2020, 2021).

86 Cloud-scale updraft velocity (i.e., the part of the vertical velocity spectrum with positive
87 values) is the major driver of droplet formation, owing to the supersaturation generated from
88 adiabatic expansion and cooling (e.g., Nenes et al., 2001; Ghan et al., 2011). Despite its
89 importance, the simulation of updraft velocity by atmospheric models is rarely constrained by
90 observations, which can lead to large uncertainties in climate and numerical weather prediction
91 models (Sullivan et al., 2016, 2018). Reutter et al. (2009) pointed out that droplet formation in
92 clouds can be limited by the amount of CCN present (called the “aerosol-limited” regime), or
93 by the vertical velocity that generates supersaturation in the cloudy updrafts (called the
94 “velocity-limited” regime). Over the complex Alpine terrain, vertical motions can be
95 significantly shaped by the effects of orography (Lohmann et al., 2016). Orographic MPCs
96 have been frequently observed in the Swiss Alps under high updraft velocity conditions, where
97 supersaturation with respect to liquid water is formed faster than it is depleted by diffusional
98 and collisional ice growth processes (Korolev and Isaac, 2003) leading to persistent MPCs
99 (Lohmann et al., 2016).

100 Given the importance of droplet number for the radiative cloud properties and
101 microphysical evolution of Alpine MPCs, it is essential to understand the main aerosol and
102 dynamics properties that drive droplet formation. A limited number of studies exist that discuss
103 this very important topic, focusing though on liquid-phase clouds (Hammer et al., 2014, 2015;
104 Hoyle et al., 2016). Hoyle et al. (2016) showed that 79% of the variance in droplet number in
105 warm clouds formed at the high-altitude research station of Jungfraujoch in the Swiss Alps
106 (3450 m a.s.l.) is driven by variations in potential CCN concentration (i.e., aerosol particles
107 with a dry diameter >80 nm). Using a cloud parcel model, Hammer et al. (2015) also

108 investigated the influence of updraft velocity, particle concentration and hygroscopicity on
109 liquid cloud formation in the Alpine region, and found that variations in vertical wind velocity
110 have the strongest influence on the aerosol activation. Up to now we are not aware of in-situ
111 studies assessing cloud droplet closure in MPCs, where the existence of ice crystals can deplete
112 supersaturation or the low temperatures may decrease CCN activity through the formation of
113 glassy aerosol.

114 Here we analyze observational data collected as part of the Role of Aerosols and Clouds
115 Enhanced by Topography on Snow (RACLETS) field campaign, which was held in the region
116 of Davos, Switzerland, during February and March 2019. This intensive field campaign aims
117 to address questions related to the modulators of orographic precipitation, the drivers of the
118 enhanced ice-crystal number concentrations observed in MPCs as well as the human-caused
119 pollution effects on cloud microphysical and optical properties. Through this study we focus
120 on a two-week period seeking to unravel the complex aerosol-droplet-updraft velocity
121 interactions that occur in the orographic MPCs. For this, we combine CCN number
122 concentrations with the particle size distributions to understand the variations in hygroscopicity
123 over time and for sites located in the valley and a close by mountain-top site. The in-situ
124 measurements are subsequently coupled with a state-of-the art droplet parameterization to
125 determine the potential droplet numbers and the corresponding maximum supersaturation
126 achieved in cloudy updrafts. The predicted droplet numbers are evaluated against direct
127 observations, and the degree to which droplet formation is velocity- or aerosol-limited is
128 determined for the whole timeseries.

129

130 **2. Methods**

131 2.1 Observational datasets

132 This analysis utilizes measurements collected during the RACLETS campaign, which took
133 place from 8 February to 28 March 2019 ([https://www.envidat.ch/group/about/raclets-field-](https://www.envidat.ch/group/about/raclets-field-campaign)
134 [campaign](https://www.envidat.ch/group/about/raclets-field-campaign)) (Mignani et al., 2021; Ramelli et al., 2021a, b; Lauber et al., 2021). This joint
135 research project offers a unique dataset of orographic clouds, precipitation and snow
136 measurements in an effort to shed light on some fundamental microphysical processes being
137 present in subsequent stages of the lifecycle of clouds (i.e., cloud formation, precipitation onset,
138 cloud dissipation). All measurements presented in this paper were performed at two distinct
139 observation stations near Davos, Switzerland (supplement Fig. S1). A measurement site is
140 located at Davos Wolfgang, which is the pass between Davos (1560 m a.s.l.) in the South and

141 Klosters (1200 m a.s.l.) in the North and is otherwise known as Wolfgang-Pass (WOP; 1630
142 m a.s.l., 46°50'08.076"N 9°51'12.939"E). Measurements were also conducted at the mountain-
143 top station Weissfluhjoch (WFJ; 2700 m a.s.l., 46°49'58.670"N 9°48'23.309"E), which is
144 located ~1 km above the valley floor in Davos, in the eastern part of the Swiss Alps. The
145 current study primarily focuses on data collected during a two-week period of interest, which
146 spans from 24 February to 8 March 2019. During the RACLETS campaign, a defective sheath
147 air filter affected the CCN measurements collected at WFJ, thus inhibiting data usage from the
148 instrument for a large duration of the campaign. Therefore, we limit our analysis to the above-
149 mentioned period, when the CCN counter was fully operational. Besides, during the selected
150 period two distinct weather patterns were observed (fair weather conditions interrupted by a
151 precipitating period), allowing for a contrasting analysis of the observed scenarios. The
152 following description refers to the measurements that provided the basis for the present analysis
153 (see Table 1).

154

155 *2.1.1 Aerosol particle size distribution measurements*

156 Particle size distributions were continuously monitored at WOP and WFJ using commercially
157 available Scanning Mobility Particle Sizers (SMPS; Model 3938, TSI Inc., US). At both
158 stations, the systems consisted of a differential mobility analyzer (Model 3081, TSI Inc., US),
159 a soft X-ray neutralizer (Model 3088, TSI Inc., US) and a water-based condensation particle
160 counter (Model 3787 at WOP, Model 3788 at WFJ, TSI Inc. US). Running the particle counters
161 in low flow mode (0.6 Lmin^{-1}), using a sheath flow of 5.4 Lmin^{-1} and applying a total scanning
162 time of 2 minutes (scan time: 97 s, retrace time: 3 s, purge time: 10 s), particle size distributions
163 between 11.5 nm and 469.8 nm diameter were monitored.

164

165 *2.1.2 CCN measurements*

166 A Droplet Measurement Technologies (DMT) single-column continuous-flow streamwise
167 thermal gradient chamber (CFSTGC; Roberts and Nenes, 2005) was used to carry out in-situ
168 measurements of CCN number concentrations for different supersaturations (SS). The
169 CFSTGC consists of a cylindrical flow tube with wetted walls, inside which SS is developed
170 by applying a linear streamwise temperature gradient between the column top and bottom.
171 Owing to the greater mass diffusivity of water vapor than the thermal diffusivity of air, a
172 constant and controlled SS is generated with a maximum at the centerline of the flow tube. The
173 SS is mainly dependent on the applied temperature gradient, flow rate and pressure (Roberts
174 and Nenes, 2005). An aerosol sample flow is introduced at the column centerline, and those

175 particles having a critical supersaturation lower than the instrument SS will activate to form
176 droplets and will afterward be counted and sized by an Optical Particle Counter (OPC) located
177 at the base of the CFSTGC column. The SS developed within the instrument responds linearly
178 to changes in pressure, since its operation relies on the difference between heat and mass
179 diffusivity. Calibration of the instrument, which determines the output supersaturation, was
180 performed by the manufacturer at ~ 800 mbar, while throughout the campaign the CFSTGC
181 was operating at a lower pressure ~ 735 mbar, therefore the SS reported by the instrument is
182 adjusted by a factor of $\frac{735}{800} = 0.92$, which accounts for the difference between the ambient and
183 the calibration pressure (Roberts and Nenes, 2005). CCN concentrations were measured at a
184 specific SS for approximately 10 minutes; the instrument was cycled between 6 discrete values
185 ranging from 0.09% to 0.74% supersaturations, producing a full spectrum every hour. Each 10-
186 minute segment of the raw CCN data are filtered to discount periods of transient operation
187 (during supersaturation changes), and whenever the room temperature housing the instrument
188 changed sufficiently to induce a reset in column temperature (the instrument control software
189 always sets the column temperature to be at least 1.5 degrees above the room temperature to
190 exclude spurious supersaturation generation in the column inlet). The CFSTGC was deployed
191 on the mountain-top site of WFJ with the intention of relating the CCN measurements directly
192 to the size distribution and total aerosol concentration data measured by the SMPS instrument
193 at the same station.

194

195 *2.1.3 Cloud microphysical measurements*

196 In-situ observations of the cloud microphysical properties were obtained with the tethered
197 balloon system HoloBalloon (Ramelli et al., 2020). The main component of the measurement
198 platform is the holographic cloud imager HOLIMO 3B, which uses digital in-line holography
199 to image an ensemble of cloud particles in the size range from $6 \mu\text{m}$ to 2mm diameter in a
200 three-dimensional detection volume. Note that particles smaller than $6 \mu\text{m}$ are not detected by
201 HOLIMO, which means that the droplet number concentration may be underestimated. Based
202 on a set of two-dimensional images, information about the particle position, size and shape can
203 be obtained. The detected particles can be classified as cloud droplets and ice crystals using
204 supervised machine learning (Fugal et al., 2009; Touloupas et al., 2020). The differentiation
205 between cloud droplets (circular) and ice crystals (non-circular) is done for particles exceeding
206 $25 \mu\text{m}$ diameter based on their shape (Henneberger et al., 2013). From the classification, the
207 phase-resolved size distribution, concentration and content can be derived (Henneberger et al.,

208 2013; Ramelli et al., 2020). The HoloBalloon platform was flying at WOP and provided
 209 vertical profiles of the cloud properties within the lowest 300 meters of the boundary layer
 210 (BL). The current analysis utilizes the cloud droplet number concentration and liquid water
 211 content (LWC) measurements. Note that the LWC is calculated based on the size distribution
 212 of the cloud droplets using a liquid water density (ρ_w) of 1000 kg m⁻³ and is therefore dominated
 213 by large cloud particles.

214

215 **Table 1.** Overview of data sources from the RACLETS campaign used for this study. Along
 216 with the observed parameters, the corresponding instrumentation, measurements range and
 217 time resolutions are listed.

Measured parameter	Measurement site	Instrument	Measurement range	Time resolution
Aerosol number size distribution	WOP/ WFJ	Scanning Mobility Particle Sizer	11.5 – 469.8 nm	2 min
CCN number concentration	WFJ	Continuous flow streamwise thermal gradient CCN counter	$SS = 0.09 - 0.74\%$	1 s
Cloud droplet number concentration and liquid water content	WOP	Holographic cloud imager HOLIMO	6 $\mu\text{m} - 2 \text{ mm}$	10 – 20 s
Precipitation	WOP/ WFJ	Parsivel disdrometer/ MeteoSwiss weather station	0.2 mm – 25 mm	30 s
Horizontal wind speed and direction	WOP/ WFJ	MeteoSwiss weather station	–	10-min averages
Profiles of vertical wind speed	WOP	Wind Doppler Lidar	200 m – 8100 m AGL	5 s max

218

219 2.1.4 Meteorological data

220 During the measurement period, meteorological parameters (e.g., pressure, temperature,
 221 precipitation, horizontal wind speed and direction) were continuously monitored by the

222 permanent MeteoSwiss observation station at WFJ. Additionally, a weather station was
 223 installed on the OceaNet container (Griesche et al., 2019) deployed at WOP, which also hosted
 224 several remote sensing instruments (e.g., Cloud radar, Raman Lidar, Microwave radiometer)
 225 and a Particle Size Velocity (Parsivel) disdrometer (Parsivel2, OTT HydroMet GmbH,
 226 Germany; Tokay et al., 2014) to measure precipitation. As there was no wind sensor included
 227 in the weather station on the OceaNet container, we utilized the horizontal wind speed and
 228 direction measurements from the nearby MeteoSwiss station in Davos, assuming that they
 229 provide a good proxy for the wind regime in the valley. Vertical wind speed profiles were
 230 obtained with a wind Doppler Lidar (WindCube 100S, manufactured by Leosphere) at WOP.
 231 Throughout the campaign the wind lidar measured from 200 m to 8100 m above ground level
 232 (AGL) with high temporal (5 s max) and vertical resolution (50 m). The wind lidar operated
 233 following the Doppler Beam Switching technique with an elevation of 75°. More information
 234 about the remote sensing measurements can be found in Ramelli et al. (2021a).

235

236 2.2 Aerosol hygroscopicity

237 The aerosol hygroscopicity parameter, κ , encompasses the impact of particle chemical
 238 composition on its subsaturated water uptake and CCN activity (Petters and Kreidenweis,
 239 2007). Here, we determine κ similar to the approach of Moore et al. (2011), Jurányi et al.
 240 (2011), Latham et al. (2013), Kalkavouras et al. (2019), Kacarab et al. (2020) and others, by
 241 combining the CCN measurements with the SMPS aerosol size distribution data as follows.
 242 For each SMPS scan, the particle size distribution is integrated backward starting from the bin
 243 with the largest-size particles – which corresponds to CCN with the lowest critical
 244 supersaturation, S_{cr} . We then successively add bins with smaller and smaller diameters, until
 245 the aerosol number matches the CCN concentration observed for the same time period as the
 246 SMPS scan. The particles in the smallest size bin, which we call *critical dry diameter*, D_{cr} ,
 247 correspond to CCN with highest S_{cr} possible – being the instrument supersaturation, SS . From
 248 D_{cr} and SS we determine κ from Köhler theory (Petters and Kreidenweis, 2007), assuming the
 249 particle chemical composition is internally mixed:

$$\kappa = \frac{4A^3}{27D_{cr}^3 SS^2} \quad (1)$$

250 where $A = \frac{4M_w\sigma}{RT\rho_w}$ is the Kelvin parameter, in which M_w (kg mol⁻¹) is the molar mass of water, σ
 251 (J m⁻²) is the surface tension of the solution droplet, R is the universal gas constant and T (K)
 252 is the ambient temperature. Here we assume the surface tension of the solution droplet is equal

253 to that of pure water ($\sigma = \sigma_w$) by convention. The κ determined above represents the composition
 254 of particles with diameter D_{cr} (large particles can have a different κ but still activate given that
 255 their S_{cr} is lower than the prevailing SS in the CCN chamber). This means that over the course
 256 of an hour, over which a full SS cycle is completed, κ is determined for a range of D_{cr} , which
 257 in our case were in the range of 50-200 nm (Section 3.1). This size-resolved κ information
 258 provides insights on the possible origin and chemical components of the aerosol, which is
 259 important given that there is no other measurement available to constrain chemical composition
 260 during RACLETS. From κ , we infer an equivalent organic mass fraction, ϵ_{org} , assuming that
 261 the aerosol is composed of an organic-inorganic mixture:

$$\epsilon_{org} = \frac{(\kappa - \kappa_i)}{(\kappa_o - \kappa_i)} \quad (2)$$

262 where $\kappa_i = 0.6$ and $\kappa_o = 0.1$ are characteristic hygroscopicity values for the inorganic fraction
 263 of aerosol (represented by ammonium sulphate), and organic aerosol, respectively (Petters and
 264 Kreidenweis, 2007; Wang et al., 2008; Dusek et al., 2010). Note that these values for a
 265 continental aerosol are supported by observations and analyses (e.g., Andreae and Rosenfeld,
 266 2008; Rose et al., 2008; Pringle et al., 2010).

267

268 2.3 Cloud droplet number and cloud maximum supersaturation

269 Here we apply adiabatic cloud parcel theory to the observational datasets to determine the
 270 maximum in-cloud supersaturation (S_{max}) and cloud droplet number (N_d) that would form over
 271 both measurement sites throughout the observation period. Droplet calculations are carried out
 272 with the physically based aerosol activation parameterization of Nenes and Seinfeld (2003),
 273 with extensions introduced by Fountoukis and Nenes (2005), Barahona et al. (2010), and
 274 Morales and Nenes (2014). Each N_d calculation requires knowledge of the observed pressure,
 275 temperature, vertical winds, aerosol size distribution and hygroscopicity. For the WFJ site, all
 276 data are available as described in the sections above. For the WOP site, CCN (hence
 277 hygroscopicity) data are not available, so we carry out N_d calculations at two κ values, 0.1 and
 278 0.25, which is the upper and the lower limit determined from the WFJ analysis (Section 3.1).
 279 The ability to reproduce observed cloud droplet number concentrations (“Method evaluation
 280 against direct observations”, Section 3.2.1) further supports the selection of these values.

281 The wind lidar measurements conducted at WOP (Section 2.1.4) are used to determine
 282 the prevailing vertical velocities at both sites. Data extracted from the first bin of the lidar,
 283 being 200 m AGL, are considered representative for WOP as the wind lidar has no values very

284 close to the ground, while measurements extracted for 1100 m AGL are used as a proxy for the
285 vertical velocities at WFJ. The high resolution wind lidar data are grouped by hour and each
286 fitted to half-Gaussian probability density functions (PDFs) with zero mean and standard
287 deviation σ_w . An hourly PDF of updraft velocities is provided in the supplementary material as
288 an example of the calculation method we followed here (supplement Fig. S2). Employing the
289 “characteristic velocity” approach of Morales and Nenes (2010), the PDF-averaged values of
290 N_d and S_{max} are calculated by applying the parameterization using a single characteristic
291 velocity, $w^*=0.79\sigma_w$. This approach has been shown to successfully predict cloud-scale values
292 of N_d in field studies for cumulus and stratocumulus clouds (e.g., Conant et al., 2004;
293 Meskhidze et al., 2005; Fountoukis et al., 2007; Kacarab et al., 2020). The droplet closure
294 carried out in this study is also used to support the validity of this approach for Alpine MPCs.
295 To determine the σ_w values used in the closure study (Section 3.2.1), we isolated the segments
296 of the wind lidar measurements that correspond to each cloud event observed by the
297 Holoballoon platform. The subsequent fitting of the measured updraft velocities to half-
298 Gaussian PDFs revealed a σ_w value representative of each cloud. The accuracy of the wind lidar
299 products is affected by precipitation, as the measured updraft velocities might be masked by
300 the terminal fall velocity of the hydrometeors. We therefore use disdrometer measurements to
301 identify and exclude precipitating periods from our analysis. Aiming to examine how N_d
302 responds to different vertical velocity-aerosol situations, as a sensitivity test, potential N_d for
303 both sites are calculated at 10 values of σ_w between 0.1 and 1.0 ms^{-1} that cover the observed
304 range (Section 3.2.4). Note that we use the term “potential” droplet number throughout this
305 study, as its calculation is performed regardless of the actual existence of clouds over the
306 measurement sites.

307

308 **3. Results and discussion**

309 **3.1 Particle number, CCN concentration and κ at WOP and WFJ**

310 The total aerosol number concentration (N_{aer}) timeseries (integrated aerosol size distribution)
311 together with horizontal wind speed and direction measurements are depicted for both sites in
312 Figure 1. The N_{aer} data points of WFJ are colored by κ (Section 2.2), while the orange solid
313 line is used as a trace for WOP timeseries, as κ was not determined for the site owing to a lack
314 of corresponding CCN measurements. Aiming to interpret the aerosol variations and the
315 potential differences observed between valley and high-altitude measurements, the two-week
316 period of interest is divided into two different sub-periods. During 24 and 28 of February, a

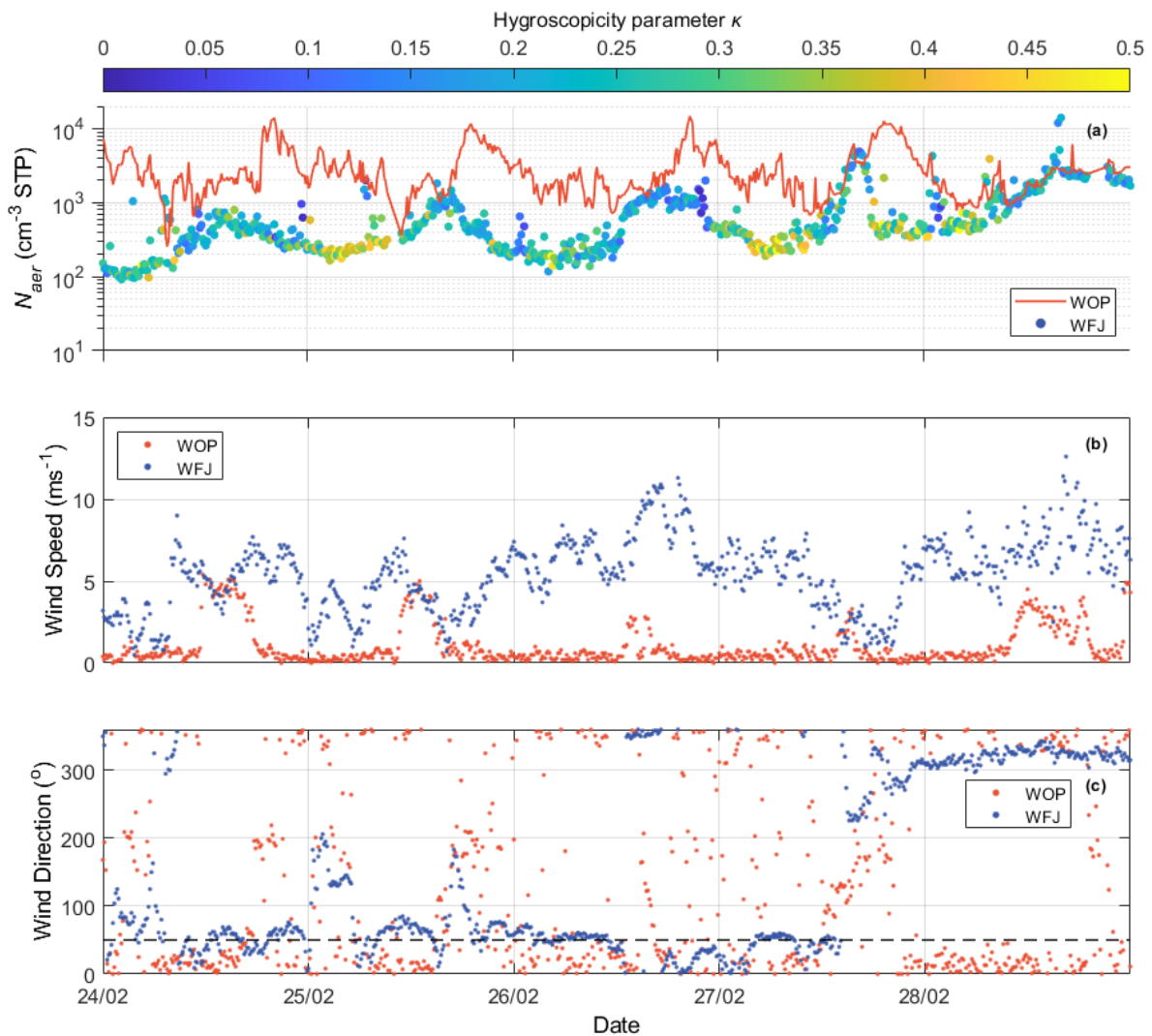
317 high-pressure system was dominant over Europe with clear skies and elevated temperatures
318 (supplement Fig. S3). During this first sub-period, the N_{aer} varies considerably, and tends to
319 follow a diurnal cycle that anticorrelates between the two sites (Fig. 1a). The concentrations at
320 WOP are most of the times elevated with respect to WFJ, which is expected as the N_{aer} in the
321 valley is higher – being influenced by local sources, which during this time of the year include
322 emissions from biomass burning (BB) (Lanz et al., 2010). N_{aer} at WOP peaks in the evening,
323 reaching up to $\sim 10^4 \text{ cm}^{-3}$ presumably because of BB emissions in the valley which seem to
324 stop around midnight (Fig. 1a). Up to 2 orders of magnitude lower N_{aer} is measured at the same
325 time at the WFJ site. In the afternoon, aerosol concentrations at WFJ approach those observed
326 at WOP, indicating that the two sites are possibly experiencing similar air masses. The κ for
327 WFJ seems to follow a clear temporal pattern as well, ranging between $\sim 0.1-0.4$ with a
328 minimum in the afternoon, when the two sites experience the same air masses. Low N_{aer} values
329 are accompanied by higher κ , while at higher N_{aer} conditions less hygroscopic aerosols are
330 recorded (Fig. 1a).

331 The above diurnal cycles and their relationships can be understood in terms of BL
332 dynamics typically occurring in mountain-valley systems (Chow et al., 2013). During daytime,
333 under clear sky conditions, the slopes and the valley itself are warmed by solar radiation,
334 causing rising of the BL, and additionally the production of buoyant air masses that rise up the
335 slope toward the summit (through “up-slope” and “up-valley” winds) (Okamoto and Tanimoto,
336 2016). This hypothesis can be further supported by the fair weather recorded by the weather
337 station at WFJ until 28 February (supplement Fig. S3). The buoyant upslope flow could then
338 transport polluted air masses originating from the BL of the valley up to the WFJ site, elevating
339 the concentrations of less hygroscopic aerosols observed in the afternoon. The situation
340 reverses during nighttime, when cold air descends from the slopes (down-slope winds) and
341 flows out of the valley (down-valley winds) due to the radiative cooling of the surface. The
342 less polluted air observed during the early hours of the day before sunrise indicates that the
343 WFJ station remained in the free troposphere (FT), with lower N_{aer} and more aged air (i.e.,
344 larger κ) with a more prominent accumulation mode (Baltensperger et al., 1997; pp. 376-378
345 in Seinfeld and Pandis, 2006; Kammermann et al., 2010; Jurányi et al., 2011).

346 Another consideration is that the upslope flow that “connects” the valley and the
347 mountain-top site may not only be driven by thermal convection but also from mechanically-
348 forced lifting. The latter mechanism is caused by the deflection of strong winds by a steep
349 mountain slope and it can be of great importance depending mainly on the height of the
350 mountain and the mean speed of the wind (Kleissl et al., 2007). The local wind effects can be

351 further interpreted looking at the MeteoSwiss timeseries of wind speed and direction for both
 352 stations (Fig. 1b, c). Wind measurements at WFJ station recorded a strong wind speed reaching
 353 up to $\sim 11 \text{ ms}^{-1}$ from easterly-northeasterly directions between 24 and 28 of February. The wind
 354 direction measured at WFJ coincides with the relative location of WOP site (see black dashed
 355 line in Fig. 1c). The steep orography over the Alps would transform part of this strong
 356 horizontal motion into vertical motion, and transport air from WOP to WFJ, as seen in other
 357 Alpine locations, like Jungfraujoch (e.g., Hoyle et al., 2016). A detailed analysis however is
 358 out of the scope of this study.

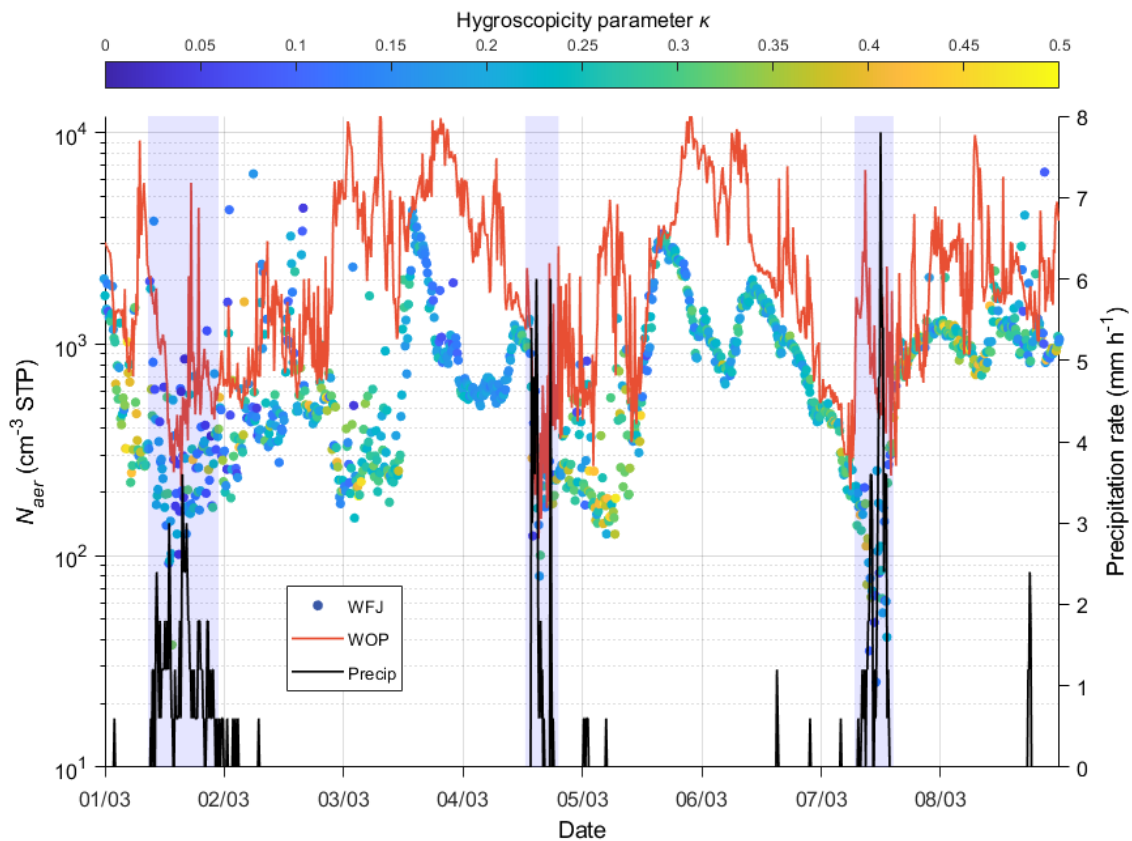
359



360

361 **Figure 1.** (a) N_{aer} in standard temperature and pressure conditions (cm^{-3} STP) at WOP (orange
 362 line) and at WFJ (circles colored by κ), (b) wind speed (ms^{-1}), and (c) wind direction (in
 363 degrees) obtained from the MeteoSwiss observation stations at WFJ (blue dots) and Davos
 364 (orange dots) between 24 and 28 February 2019. The black dashed line indicates the relative
 365 direction of WOP to WFJ. Each day is referenced to 00 UTC.

366



368

369 **Figure 2.** N_{aer} (cm^{-3} STP) at WOP (orange line) and at WFJ (circles colored by κ). The black
 370 solid line represents the precipitation rate (mm h^{-1}) recorded from the MeteoSwiss observation
 371 station for each 10-min interval at WFJ between 1 and 8 of March 2019. The blue-shaded areas
 372 represent the periods when precipitation recorded at WFJ site is most intense.

373

374

Similar to Figure 1a, Figure 2 illustrates the N_{aer} timeseries measured at both sites along
 375 with the precipitation rate recorded by the MeteoSwiss station at WFJ during the time period
 376 between 1 and 8 March 2019. Meteorological observations show the pressure and temperature
 377 dropping (supplement Fig. S3) together with intense snow and rain events, associated with the
 378 passage of cold fronts over the region. Three intense precipitation events are visible in our
 379 dataset occurring on the 1st, 4th and 7th of March 2019 (blue-shaded areas on Fig. 2) creating
 380 up to 7.8 mm per hour of precipitation. The most intense drop in N_{aer} is seen to occur during
 381 and after the precipitation events, with the aerosol concentrations dropping to less than 200 cm^{-3}
 382 (100 cm^{-3}) at WOP (WFJ). This is not the case for the last event, where a big “spike” of N_{aer}
 383 is observed before the precipitation event in WOP timeseries, which is in contrast with the
 384 concurrent sharp decrease in N_{aer} ($< 20 \text{ cm}^{-3}$) observed at WFJ. This could be an indication of
 385 a local source affecting the N_{aer} recorded in the valley. During dry weather conditions, we can
 386 notice again the aerosol timeseries correlating during the afternoon and anticorrelating later in

387 the evening-early morning hours. On March 3, a steep increase in N_{aer} is seen in WFJ timeseries
388 reaching up to $\sim 4000 \text{ cm}^{-3}$, which is followed by a period of several hours with low
389 hygroscopicity values ($\kappa < 0.2$) indicating once more the influence of freshly emitted particles
390 arriving at WFJ from the BL of lower altitudes. Additionally, between 1 and 8 March, the
391 diurnal cycle of particle hygroscopicity is less pronounced compared to the period between 24
392 and 28 February. Especially on the 1st and 7th of March, less hygroscopic aerosols ($\kappa < 0.1$) –
393 hence less effective CCN particles – are found at WFJ (Fig. 2). This is likely from either
394 precipitation removing aerosol through diffusive and impaction processes, or, the removal of
395 aerosol particles that first activate and then are removed by precipitation. Also, because N_{aer}
396 drops, fresh local emissions become more important, further justifying the predominance of
397 low hygroscopicity values.

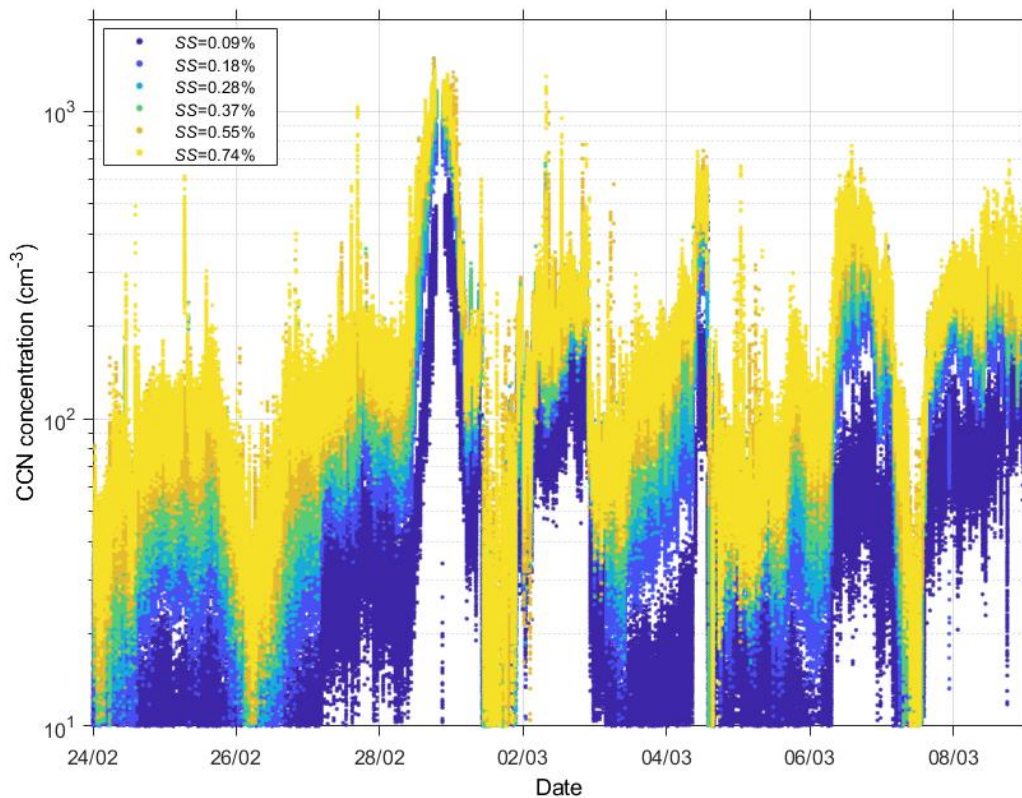
398 Figure 3 presents the CCN number concentration timeseries measured at ambient
399 conditions at WFJ for all 6 supersaturations. Throughout the two-week measurement period
400 the recorded CCN number concentrations do not seem to follow a clear temporal pattern. The
401 absence of a diurnal cycle in CCN properties measured at Jungfraujoeh during winter was also
402 pointed out in the study of Jurányi et al. (2011), because the site is mainly in free tropospheric
403 conditions during most of the winter. According to Figure 3, the observed CCN concentrations
404 tend to be low ($\sim 10^2 \text{ cm}^{-3}$) even at the highest SS (0.74%), which is expected given that WFJ
405 is a remote continental measurement site with CCN concentrations that are typical of free
406 tropospheric continental air (Jurányi et al., 2010, 2011; Hoyle et al., 2016; Fanourgakis et al.,
407 2019). This is again in line with the measured monthly median values of CCN (at $SS = 0.71\%$)
408 reported by Jurányi et al. (2011) being equal to 79.1 and 143.4 cm^{-3} for February and March
409 2009, respectively. Some local CCN spikes are however recorded during the evening of 28
410 February and at the beginning of March (e.g., on 2nd, 4th and 6th March), with the observed
411 values of CCN reaching up to 650 cm^{-3} at $SS=0.09\%$ (lowest SS) and 1361 cm^{-3} at $SS=0.74\%$
412 (highest SS). Considering that WFJ is a site frequently located in the FT, sudden fluctuations
413 in the CCN concentrations could be related to the vertical transport of freshly emitted particles
414 (e.g., wood burning or vehicle emissions) from the valley floor in Davos. It is also worthy to
415 note that some aerosol spikes observed on the 3rd ($\sim 3350 \text{ cm}^{-3}$) and the 5th of March (~ 2100
416 cm^{-3}) in the WFJ timeseries (Fig. 1a) are not accompanied by a corresponding peak in the CCN
417 timeseries. This indicates the presence of small aerosol particles, which activate above 0.74%
418 supersaturation (i.e., particles with a diameter smaller than $\sim 25 \text{ nm}$). This event could also be
419 associated with new particle formation (NFP) events. A previous study by Herrmann et al.

420 (2015) reported the aerosol number size distribution at the Jungfraujoch over a 6-year period
 421 indicating that NPF was observed during 14.5% of the time without a seasonal preference.
 422 Tröstl et al. (2016) also showed that NPF significantly adds to the total aerosol concentration
 423 at Jungfraujoch and is favored only under perturbed FT conditions (i.e., BL injections). Finally,
 424 during the three intense precipitation events (on 1st, 4th and 7th March) we can identify again
 425 that the wet removal of the more hygroscopic aerosol (Fig. 2) suppresses the presence of cloud-
 426 activating particles, at times depleting the atmosphere almost completely from CCN (Fig. 3).
 427 This is clearly shown on the 1st and the 7th of March, when the CCN number measured at 0.74%
 428 supersaturation drops below 10 cm^{-3} , which is extremely low for BL concentrations.

429 The aerosol hygroscopicity parameter derived from all CCN data collected between 24
 430 February and 8 March is presented in Figure 4a. The red solid line represents the hourly
 431 averaged hygroscopicity values over one complete instrument supersaturation cycle. The
 432 hygroscopic properties of the particles at WFJ vary as a function of supersaturation, exhibiting
 433 on average lower values (~ 0.1) at high *SS* and higher values (~ 0.3) at the lower *SS*. Since the
 434 supersaturation inversely depends on particle size, Figure 4a indicates that the hygroscopicity
 435 of the particles drops by almost 60% as the particles are getting smaller (i.e., as the
 436 supersaturation increases). Table 2 summarizes the mean values of κ and D_{cr} and their standard
 437 deviations, as calculated for each measured *SS*. The anticorrelation seen between the instrument
 438 *SS* and D_{cr} is reasonable, if we consider that the latter represents the minimum activation
 439 diameter in a population of particles, and therefore only the particles with a $D_{cr} > 193.54 \text{ nm}$
 440 are able to activate into cloud droplets at low *SS* values (0.09%). The hourly averaged κ at each
 441 *SS* slot falls within a range of ~ 0.2 and ~ 0.3 , which is a well representative value of continental
 442 aerosols (Andreae and Rosenfeld, 2008; Rose et al., 2008).

443 **Table 2.** Average κ and D_{cr} values at WFJ for each *SS* measured between 24 February and 8
 444 March 2019. Uncertainty for each value is expressed by the standard deviation.

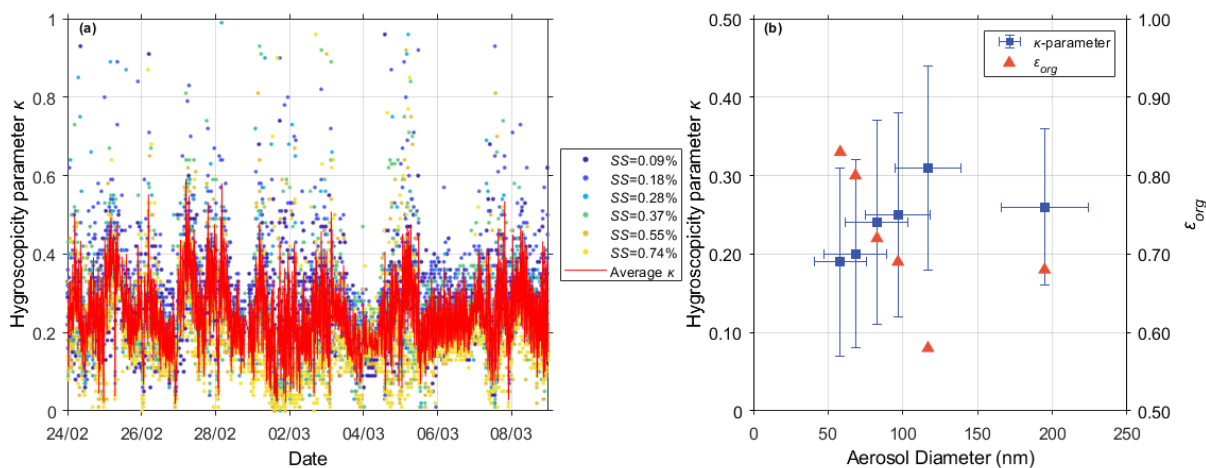
<i>SS</i> (%)	κ_{mean}	$D_{cr,mean}$
0.09	0.26 ± 0.10	193.54 ± 29.58
0.18	0.31 ± 0.13	116.80 ± 22.20
0.28	0.25 ± 0.13	96.69 ± 21.62
0.37	0.24 ± 0.13	82.67 ± 20.93
0.55	0.20 ± 0.12	68.30 ± 20.95
0.74	0.19 ± 0.11	58.11 ± 17.54



446

447 **Figure 3.** Timeseries of in-situ CCN number concentrations (cm^{-3}) at WFJ for different levels
 448 of supersaturation (SS) with respect to water between 24 February and 8 March 2019.

449



450

451 **Figure 4.** (a) Timeseries of the hygroscopicity parameter κ at WFJ at different levels of SS
 452 (0.09–0.74%) throughout the period of interest. The red solid line indicates the hourly averaged
 453 κ timeseries over a complete SS cycle. (b) Size-resolved aerosol hygroscopicity (blue squares)
 454 and the respective ϵ_{org} (orange triangles) calculated for the WFJ site.

455

456 The hygroscopicity parameter κ along with the inferred ε_{org} (Eq. 2) are shown in Figure
457 4b as a function of particle size. Compared to smaller particles, the higher κ of larger particles
458 (>100 nm) is consistent with them being more aged and with a lower fraction of organics. The
459 smaller particles are possibly enriched in organic species, which is consistent with the notion
460 that air masses in the valley can contain large amounts of freshly emitted BB smoke with lower
461 κ . Aerosol particles in the FT are considerably more aged (pp. 376-378 in Seinfeld and Pandis,
462 2006) and exhibit higher values of κ and consequently lower values of ε_{org} . The chemical
463 composition of sub-100 nm particulate matter was therefore presumably dominated by organic
464 material transported from the valley, while the higher κ values characterizing the larger
465 particles are consistent with the more aged character of free tropospheric aerosols (e.g., Jurányi
466 et al., 2011). The higher ε_{org} inferred for the smaller particles suggests that mixing between
467 fresh emissions in the valley and the free tropospheric aerosol might also be taking place at
468 WFJ.

469

470 3.2 Droplet formation in the Alpine region

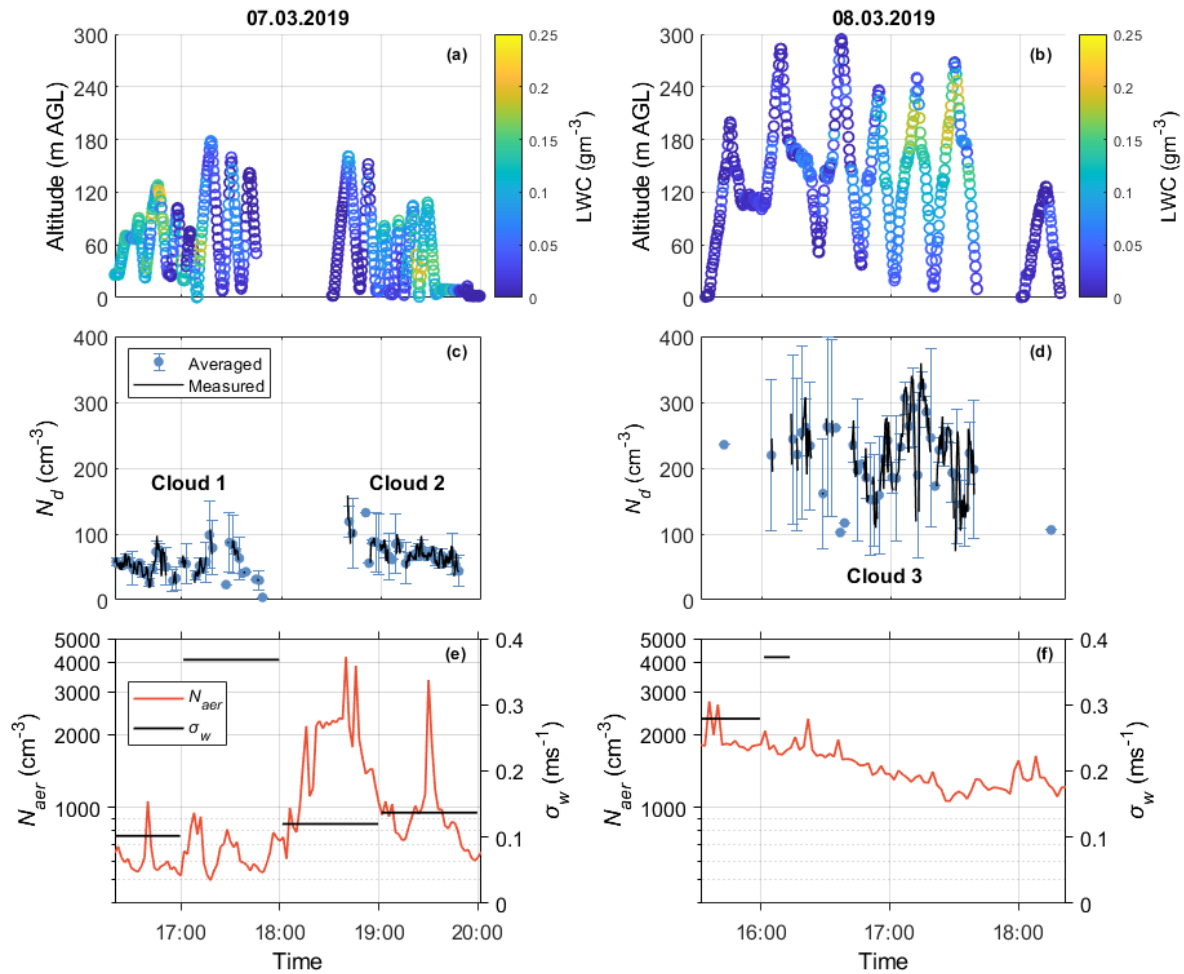
471 3.2.1 Method evaluation against direct observations

472 During the RACLETS campaign, planar and dendritic ice particles were collected from
473 supercooled clouds at WFJ aiming to examine their refreezing ability. A detailed description
474 of the sampling methodology can be found in Mignani et al. (2019). Between 1 and 7 March,
475 images of single dendrites were taken and analyzed visually for the degree of riming
476 (supplement Fig. S4). The estimated riming degree varies from 1 (lightly-rimed) to 4 (heavily-
477 rimed) following the categorization of Mosimann et al. (1994). Some representative images of
478 each measured riming degree are shown in Figure S4b. Although images were captured
479 intermittently, they were taken within all three intense precipitating events occurring during
480 the period of interest (blue-shaded areas on Fig. 2). All dendrites captured were at least lightly
481 rimed (i.e., riming degree = 1), which provides direct evidence for the co-existence of
482 supercooled droplets and ice in clouds. Except the indirect evidence of the presence of MPCs
483 over WFJ, Figure 5 provides an overview of the direct microphysical measurements carried
484 out by the Holoballoon at WOP (Section 2.1.3). Three cloud events are sampled during the 7th
485 and the 8th of March, a more detailed description of which can be found in Ramelli et al. (2021a,
486 b). The observed low-level clouds are likely produced by orographic lifting when the low-level
487 flow is forced to ascent over the local topography from Klosters to WOP producing local
488 updrafts and thus water supersaturated conditions. The cloud LWC measurements from the

489 holographic imager display significant temporal variability that is also related to variations in
490 the altitude of the tethered balloon system, as it tends to follow an adiabatic profile (Fig. 5a,
491 b). Deviations from the adiabatic LWC profile are likely caused by entrainment of dry air
492 within the low-level clouds. Departures during the mixed-phase conditions recorded on March
493 8 (Fig. 5b), could also be attributed to the depletion of N_d through riming and depositional
494 growth. These two processes are frequently found to enhance orographic precipitation in feeder
495 clouds. Indeed, a large fraction of rimed ice particles and graupel were observed that day with
496 HOLIMO between 17:00 and 17:40 UTC (Ramelli et al., 2021b). Throughout the two-day
497 dataset presented in Figure 5, the HoloBalloon system samples at altitudes lower than 300 m
498 AGL, providing observations that are representative of BL conditions.

499 The observed N_d timeseries collected at WOP are illustrated in Figures 5c and 5d. The
500 measurements corresponding to $LWC < 0.05 \text{ gm}^{-3}$ are filtered out from the analysis, assuming
501 that they do not effectively capture in-cloud conditions. A similar criterion for LWC was also
502 applied in Lloyd et al. (2015) to determine the periods when clouds were present over the
503 Alpine station of Jungfraujoch. Since the measured cloud properties have finer resolution (10-
504 20 secs) than the predicted ones, the observed dataset is averaged every 2 minutes. On March
505 7, the balloon-borne measurements were taken in a post-frontal air mass (i.e., passage of a cold
506 front in the morning) and indicated the formation of two low-level liquid layers (Fig. 5c) over
507 WOP, which is attributed to low-level flow blocking (Ramelli et al., 2021a). Note that small
508 droplets ($< 6 \mu\text{m}$) cannot be detected by HOLIMO (Section 2.3.1) and therefore the reported
509 N_d should be considered as a lower estimate. The influence of small cloud droplets, however,
510 on the reported LWC is minor, since the contribution of the larger cloud droplets dominates.
511 During the first cloud event, an N_d of up to $\sim 100 \text{ cm}^{-3}$ was recorded, while slightly increased
512 N_d in the range of $\sim 50\text{-}120 \text{ cm}^{-3}$ is visible during the second cloud event. On March 8, a small-
513 scale disturbance passed the measurement location Davos, which brought precipitation
514 (Ramelli et al., 2021b). During the passage of the cloud system, the in-situ measurements
515 collected at WOP revealed the presence of a persistent low-level feeder cloud confined to the
516 lowest 300 m of the cloud. The mixed-phase low-level cloud that is shown in Figure 5d, turned
517 into an ice-dominated low-level cloud after 18 UTC (not shown). Throughout this event, N_d
518 seems to range between $\sim 100\text{-}350 \text{ cm}^{-3}$ (Fig. 5d), while the observed ICNC was in the range
519 of $\sim 1\text{-}4 \text{ L}^{-1}$ (see Fig. 6b in Ramelli et al., 2021b).

520



521

522 **Figure 5.** Timeseries of the 7th (left panels) and the 8th (right panels) of March, showing the
 523 vertical profiles of the LWC (gm⁻³) in (a) and (b), the filtered (black lines) and the 2-minute
 524 averaged (cyan circles) N_d (cm⁻³) measured at WOP with the HoloBalloon platform in (c) and
 525 (d), and the corresponding SMPS aerosol concentrations (cm⁻³) (orange line) and the hourly
 526 wind-lidar derived σ_w values (ms⁻¹) (black line) in (e) and (f). Error bars represent the standard
 527 deviation of N_d during the averaging period.

528

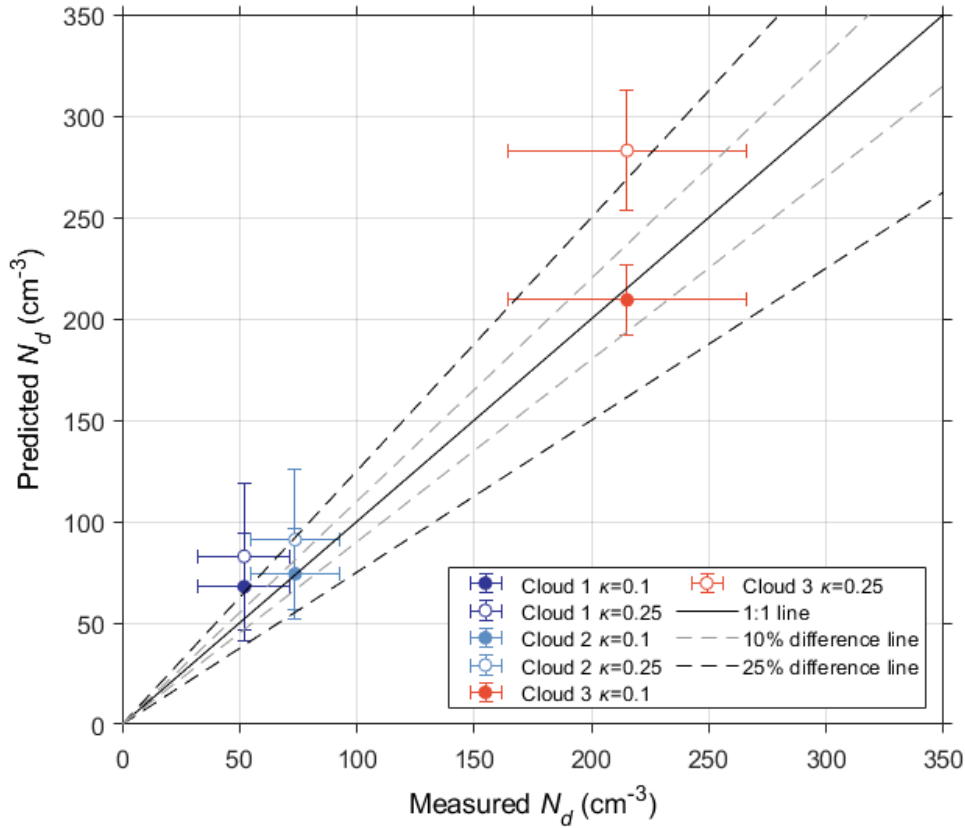
529 According to Figures 5e and 5f, low N_{aer} (<10³ cm⁻³) and highly variable σ_w values (~4
 530 times higher σ_w after 17:00) are representative of the period throughout which the first cloud
 531 formed, while up to 4 times higher N_{aer} is observed during the following two cloud events, with
 532 relatively low σ_w values characterizing the second cloud compared to the third one. On March
 533 8, the disdrometer recorded rainfall over WOP, starting a few minutes after the development
 534 of the observed cloud system, reflected in the removal of updraft velocity measurements after
 535 16:15 (Fig. 5f). Note that the concentration measurements presented in Figure 5 correspond to
 536 ambient temperature and pressure conditions. The contrasted aerosol and vertical velocity
 537 regimes, in which the observed clouds are formed, offer a great opportunity to test how the
 538 proposed methodology performs under a wide range of aerosol and velocity conditions. Indeed,

539 the mean cloud droplet diameters exhibit a wide range of values, which for WOP range between
540 10 μm and 17 μm on March 7, and 8 μm to 12 μm on March 8 (not shown).

541 The N_d closure performed for the three cloud events observed over WOP during the last
542 two days of the period of interest is presented in Figure 6. Note that the predicted N_d is
543 evaluated using the updraft velocity PDF calculated for each cloud period, rather than the
544 hourly σ_w data shown in Figures 5e and 5f (Section 2.3). Owing to the precipitation occurrence
545 during March 8, we focused on the 15-min time period between 16:00 and 16:15 to determine
546 a relevant updraft velocity from the wind lidar measurements representative of Cloud 3. The
547 Gaussian fit to the updraft velocities gave a distribution with $\sigma_w = 0.24$ and 0.16 ms^{-1} for the
548 first two clouds present on the 7th of March, and, $\sigma_w = 0.37 \text{ ms}^{-1}$ for the cloud system observed
549 on the 8th of March. The w^* values used to apply the droplet parameterization are therefore
550 between 0.1-0.4 ms^{-1} (Section 2.3). Figure 6 indicates that the parameterization predictions
551 agree to within 25% with the in-situ cloud droplet number concentrations. A similar degree of
552 closure is frequently obtained for other in-situ studies (e.g., Meskhidze et al., 2005; Fountoukis
553 et al., 2007; Morales et al., 2011; Kacarab et al., 2020), which however focused on liquid-phase
554 clouds. Here we show that the methodology can also work for MPCs (i.e., Cloud 3 in Fig. 6).
555 It is important to note here that part of the discrepancy between prediction and measurement
556 could also be related to the underestimation of the measured N_d (Section 2.1.3). Hence, an even
557 better degree of closure is likely. Also, the derived σ_w value used to calculate the predicted N_d
558 for Cloud 1, might be biased low by the lower σ_w values recorded before 17:00 (Fig. 5e).
559 Nevertheless, the updraft averaging used in the droplet closure study corresponds to the
560 measured N_d averaging time period, and therefore, we do not expect the degree of closure to
561 be affected.

562 The good agreement between measurements and predictions – even under mixed-phase
563 conditions, reveals that processes like condensation freezing and the removal of cloud droplets
564 through riming and collision-coalescence for the clouds considered are not disturbing the S_{max}
565 and hence the N_d predicted by the parameterization, at least for the given clouds. That said, it
566 is known that pre-existing liquid and ice hydrometeors falling to the activation region of clouds
567 can deplete the supersaturation affecting the number of the activated droplets – and such
568 supersaturation depletion effects can be included in the droplet activation parameterization
569 (Sud et al., 2013; Barahona et al., 2014) if needed. Furthermore, the parameterization
570 predictions indicate that the best fit is achieved using a κ of ~ 0.1 (Fig. 6). N_{aer} at WOP is likely
571 dominated by lower κ values, indicating that the particles are getting richer in organic material,
572 compared to WFJ, which supports the aerosol analysis carried out in Section 3.1. These results

573 are robust, indicating that for non-precipitating BL clouds the proposed calculation method
 574 captures cloud droplet formation at WOP and WFJ.
 575



576
 577 **Figure 6.** Comparison between average predicted N_d (cm^{-3}) with the droplet activation
 578 parameterization and N_d (cm^{-3}) observed during the three cloud events on the 7th (blue and cyan
 579 circles) and the 8th of March (orange circles) 2019. For all three cloud events droplet closure is
 580 performed assuming a κ parameter of 0.1 (filled circles) and 0.25 (empty circles). The error
 581 bars represent the standard deviation of N_d during each cloud event.

582
 583 **3.2.2 Potential droplet formation at WOP and WFJ**

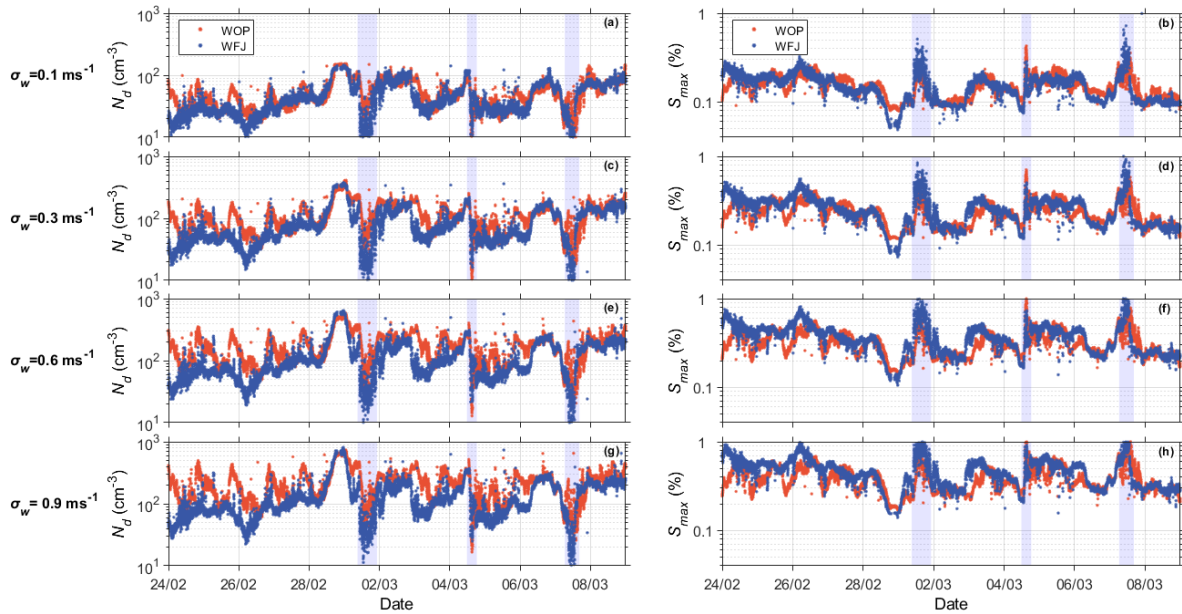
584 According to the methodology proposed in Section 2.3, using the in-situ measured N_{aer} , the
 585 estimated chemical composition and the observed updraft velocity range, we determine the
 586 potential N_d and S_{max} that would form over both measurement sites. At WOP, clouds are formed
 587 locally due to the local topography (Ramelli et al., 2021a, b), supporting the use of surface
 588 measured aerosol to estimate the potential N_d over this site. This is further supported by the
 589 good degree of droplet closure (Section 3.2.1). A similar closure study could not be repeated
 590 for WFJ owing to a lack of in-situ data, however the airmasses sampled (i.e., those given as
 591 input to the parameterization) are often in the FT, so they should contain the same aerosol as
 592 the one used to form the clouds. This does not apply under perturbed FT conditions, which are

593 however accompanied by the presence of less hygroscopic particles over the mountain-top site
594 and are less likely related to cloud formation (Section 3.1). Here we assume a κ of 0.25 to
595 calculate the potential droplets for WFJ according to our CCN-derived hygroscopicity values
596 (Table 2) and given that S_{max} usually ranges between ~ 0.1 - 0.3% . In estimating the potential
597 droplets for WOP, we use a κ of 0.1 given that aerosol is likely strongly enriched in organics;
598 the good degree of closure that this value supports its selection (Section 3.2.1). Figure 7 depicts
599 the potential N_d and the corresponding S_{max} timeseries calculated at ambient conditions for
600 WOP (orange dots) and WFJ (blue dots) using cloud updraft velocities that are indicative of
601 the observed σ_w range (Section 3.4), namely 0.1, 0.3, 0.6 and 0.9 ms^{-1} . The same behavior is
602 seen for all four σ_w values selected while, as expected, larger values of N_d and S_{max} are achieved
603 at higher σ_w . During the first days of the period of interest, the calculated N_d at WOP (Fig. 7a,
604 c, e, g) is up to 10 times larger than at WFJ, despite the lower κ values characterizing its aerosol
605 population. WFJ tends to have lower N_d due to the lower N_{aer} recorded. It is also important to
606 highlight the anticorrelation between S_{max} and N_d values arising from the nonlinear response of
607 droplet number and maximum cloud parcel supersaturation to fluctuations in the available
608 aerosol/CCN concentrations (Reutter et al., 2009; Bougiatioti et al., 2016; Kalkavouras et al.,
609 2019). Higher N_{aer} elevates N_d values. The available condensable water is then shared among
610 more growing droplets, depleting the supersaturation. Even more interesting is the fact that
611 until February 28 the calculated N_d timeseries at WOP show a pronounced diurnal cycle, similar
612 to the total N_{aer} timeseries (Section 3.1). Lower N_d values are visible after midnight, presumably
613 due to a paucity of BB activities in the valley. Droplet concentrations at WFJ do not follow a
614 diurnal pattern in contrast to the aerosol data (Fig. 1a). However, the activation fraction (i.e.,
615 N_d/N_{aer}) at WFJ displays a clear diurnal variability until the end of February (supplement Fig.
616 S5).

617 Through comparison with the MeteoSwiss precipitation measurements at WFJ (Fig. 4),
618 it should be emphasized again that during the second sub-period of interest the occurrence of
619 precipitation is followed by a depression in N_d (Fig. 7a, c, e, g) and a concurrent increase in
620 S_{max} reaching up to $\sim 1\%$ (Fig. 7b, d, f, h). Especially at WFJ, N_d drops almost to zero on the
621 1st, the 4th and the 7th of March, when precipitation is most intense (blue-shaded areas in Fig.
622 2 and 7). These trends are related to the washout of hygroscopic material observed at WFJ (Fig.
623 2) leading to the extremely low CCN concentrations ($\sim 10 \text{ cm}^{-3}$) measured during these three
624 days. During the first two intense precipitation events, the N_{aer} is relatively high, compared to
625 the third event, with concentrations reaching up to $\sim 300 \text{ cm}^{-3}$ at both stations. The small

626 activation fraction (supplement Fig. S5) combined with the high S_{max} values indicates once
 627 more that small particles that activate into cloud droplets only above 0.3 to 0.5% of
 628 supersaturation are present at both stations. However, this behavior is not seen on March 7 at
 629 WFJ.

630



631

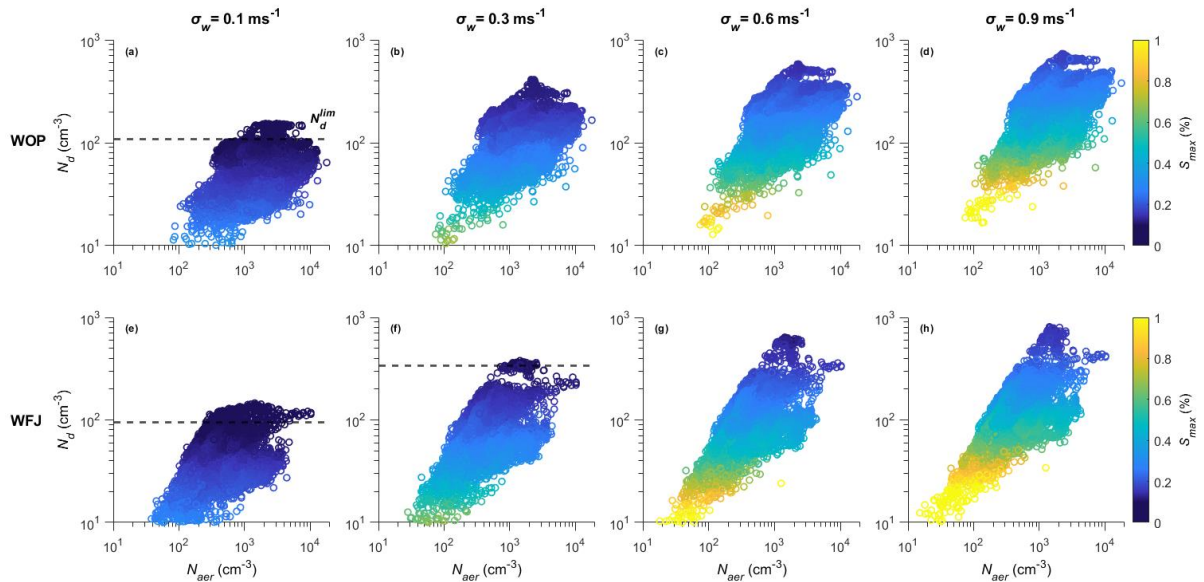
632 **Figure 7.** Calculated timeseries of N_d (cm^{-3}) (left panels) and S_{max} (%) (right panels), for updraft
 633 velocities of $\sigma_w = 0.1 \text{ ms}^{-1}$ in a and b, 0.3 ms^{-1} in c and d, 0.6 ms^{-1} in e and f, and 0.9 ms^{-1} in g
 634 and h, during the period of interest at WOP (orange dots) and WFJ (blue dots). The blue-shaded
 635 areas represent the intense precipitating periods as shown in Figure 2.

636

637 3.2.3 Droplet behavior under velocity-limited conditions

638 Combining the potential N_d and the corresponding S_{max} with the N_{aer} data yields important
 639 information on whether clouds are sensitive to vertical velocity or aerosol changes. Cloud
 640 studies (e.g., Jensen and Charlson, 1984; Twomey, 1993; Ghan et al., 1998, Nenes et al., 2001
 641 and Reutter et al., 2009) have long recognized the role of water vapor competition on droplet
 642 formation, while the success of mechanistic parameterizations for climate models relies on the
 643 ability to capture this effect accurately (e.g., Ghan et al., 2011; Morales and Nenes, 2014).
 644 Twomey (1993) discusses this conceptually and states that competition may be fierce enough
 645 to reduce N_d with increasing N_{aer} , which was later demonstrated by Ghan et al. (1998) to occur
 646 for mixtures of sulfate aerosol and sea spray. Reutter et al. (2009) did not focus on such extreme
 647 conditions of water vapor competition, but rather situations that are consistent with dominance
 648 of anthropogenic pollution in clouds. Indeed, for high N_{aer} , droplets in clouds become

649 insensitive to aerosol perturbations, giving rise to the so-called “velocity limited cloud
 650 formation”. Figure 8 displays this, presenting the response of the calculated N_d to changes in
 651 N_{aer} for a representative range of updraft velocities prevailing over WOP (top panels) and WFJ
 652 (bottom panels). The data are colored by the respective S_{max} achieved in cloudy updrafts. For
 653 low σ_w values (Fig. 8a, d) we can identify that above an N_{aer} of $\sim 300 \text{ cm}^{-3}$, the N_d at both
 654 stations reaches a plateau, where it becomes insensitive to further aerosol changes. At WFJ,
 655 the same behavior is seen for intermediate σ_w values and $N_{aer} \gtrsim 1000 \text{ cm}^{-3}$ (Fig. 8f). Kacarab et
 656 al. (2020) and Bougiatioti et al. (2020) examined a wide range of ambient size distributions
 657 and proposed that clouds became velocity-limited when S_{max} dropped below 0.1%. This reflects
 658 the increasingly fierce competition for water vapor during droplet formation, which allows only
 659 a few particles to activate into cloud droplets.
 660



661
 662 **Figure 8.** In-situ N_d (cm^{-3}) vs. N_{aer} (cm^{-3}), for updraft velocities of $\sigma_w = 0.1 \text{ ms}^{-1}$ in a and e, 0.3
 663 ms^{-1} in b and f, 0.6 ms^{-1} in c and g and 0.9 ms^{-1} in d and h, during the period of interest at WOP
 664 (top panels) and WFJ (bottom panels). Data are colored by S_{max} (%).

665
 666 Building upon these findings, we used the calculated S_{max} as an indicator for aerosol- or
 667 velocity-limited conditions prevailing over the Alps. The horizontal dashed lines plotted on
 668 Figure 8 (a), (e) and (f) illustrate a plateau, where $S_{max} < 0.1\%$ and the modulation of the N_d is
 669 driven mostly by the cloud dynamics, hence the updraft velocity variability, rather than aerosol
 670 variations. This plateau is termed limiting droplet number (N_d^{lim}), following Kacarab et al.
 671 (2020), and is essentially the maximum N_d that can be formed under these vertical velocity
 672 conditions. The vertical-velocity regime is therefore strictly defined, whenever S_{max} drops

673 below 0.1% and N_d approaches N_d^{lim} . Conversely, when S_{max} in clouds exceeds 0.1%, droplet
674 formation in the BL of both measurement sites is in the aerosol-limited regime, as the S_{max} is
675 high enough for clouds to be responsive to aerosol changes.

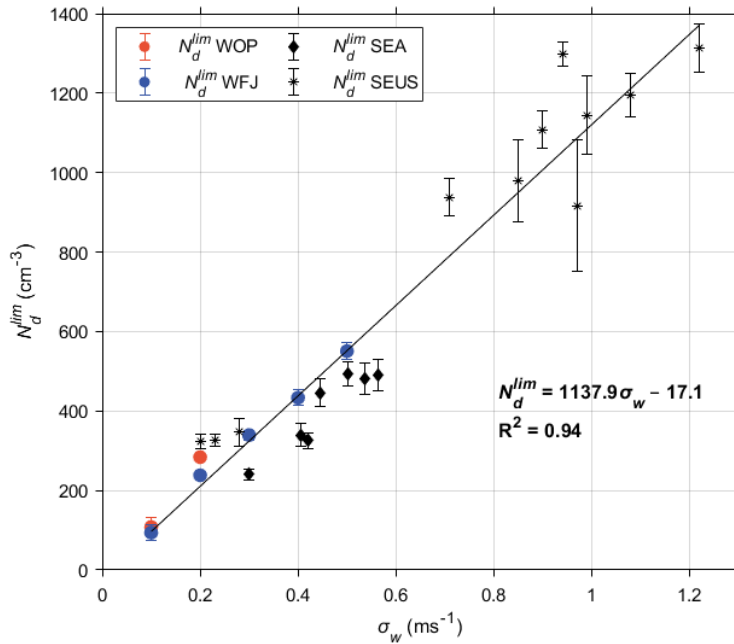
676 An alternative way of examining the N_d^{lim} response to changes in σ_w is shown in Figure
677 9. It should be noted that the N_d^{lim} values shown on this figure are determined by calculating
678 the averaged N_d achieved whenever $S_{max} < 0.1\%$ for each examined σ_w value. At WOP, droplet
679 formation is in the velocity-limited regime only for low σ_w values, namely 0.1 and 0.2 ms^{-1} ,
680 when the activated particles have more time to deplete the gas phase, and the S_{max} reached is
681 that required to activate only the largest particles. At WFJ the prevailing dynamics create
682 velocity-limited conditions even for more turbulent boundary layers when σ_w reaches up to 0.5
683 ms^{-1} . N_d^{lim} (cm^{-3}) is linearly correlated with σ_w (ms^{-1}) which can be described as $N_d^{lim} =$
684 $1137.9 \sigma_w - 17.1$ (Fig. 9). As a result, doubling σ_w from 0.1 to 0.2 ms^{-1} increases N_d^{lim} by
685 $\sim 60\%$ for both sites, while transitioning from 0.2 to 0.4 ms^{-1} further increases N_d^{lim} by $\sim 45\%$,
686 and finally an additional $\sim 20\%$ increase in N_d^{lim} occurs for WFJ for the 0.4-0.5 ms^{-1} velocity
687 range. Remarkable agreement is seen for corresponding trends between N_d^{lim} and σ_w calculated
688 for marine Stratocumulus clouds formed under extensive BB aerosol plumes over the Southeast
689 Atlantic (SEA) Ocean (Kacarab et al., 2020), along with BL clouds formed in the Southeast
690 United States (SEUS) (Bougiatioti et al., 2020). Both studies have followed the same
691 probabilistic approach for computing N_d as the one followed here. This realization is important
692 as it implies that for regions where velocity-limited conditions are expected (i.e., under
693 particularly high particle loads), $N_d \sim N_d^{lim}$ and the $N_d^{lim} - \sigma_w$ relationship can be used to
694 diagnose σ_w from retrievals of droplet number for virtually any type of BL cloud, using a
695 number of established methods (e.g. Snider et al., 2017; Grosvenor et al., 2018).

696

697 3.2.4 σ_w and observed N_d determine if droplet formation is aerosol- or velocity-limited

698 Observations of N_d when compared against N_d^{lim} can potentially be used to deduce if droplet
699 formation is velocity- or aerosol-limited. This is important because it indicates whether aerosol
700 fluctuations are expected to result in substantial N_d responses in clouds. The strong correlation
701 between σ_w and N_d^{lim} enables this comparison. From the σ_w timeseries together with the linear
702 $N_d^{lim} - \sigma_w$ relationship (Section 3.2.3; Fig. 9) we obtain estimates of N_d^{lim} for both measurement
703 stations (black dashed line in Fig. 10a, b) and the ratio N_d/N_d^{lim} (magenta dotted lines in Fig.
704 10a, b). The N_d timeseries calculated for WOP tend to be approximately one third of N_d^{lim} for

705 most of the observational period (colored circles in Fig. 10a, b), while for WFJ the same ratio
 706 is even lower $\sim 1/4$. Focusing on the relatively short periods when S_{max} values drop below 0.1%,
 707 we estimate that droplet formation over both measurement sites enters a velocity-limited
 708 regime when the ratio N_d/N_d^{lim} exceeds a critical value of 0.65, with the most prevalent value
 709 being at ~ 0.9 (supplement Fig. S6).



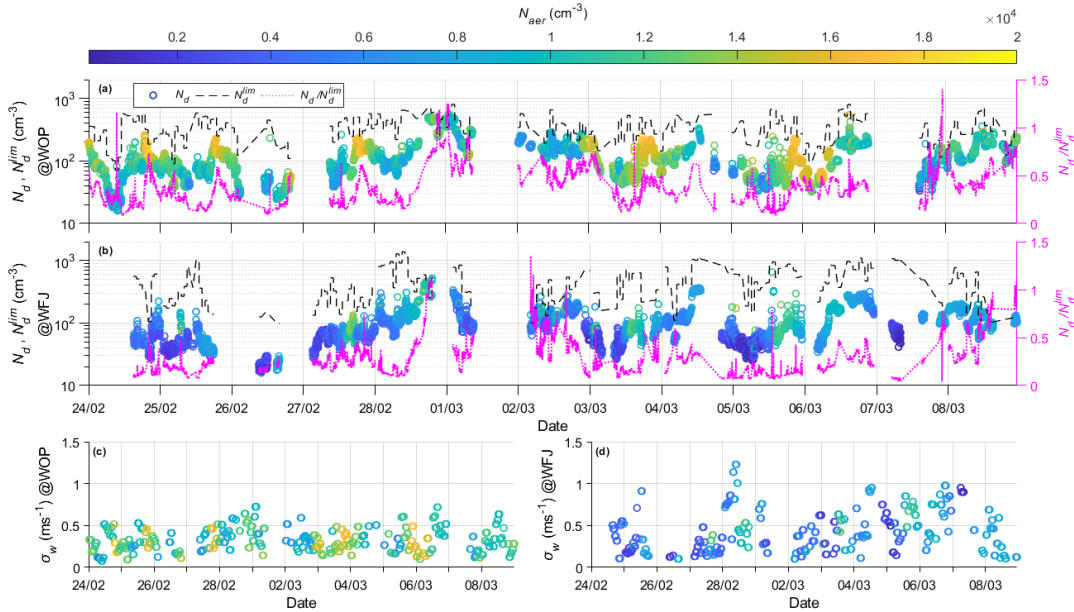
710

711 **Figure 9.** N_d^{lim} (cm^{-3}) against σ_w (ms^{-1}), calculated when velocity-limited conditions are met at
 712 WOP (orange circles) and WFJ (blue circles) throughout the period of interest. Superimposed
 713 are the corresponding values calculated for clouds forming over the SEA Ocean (rhombuses)
 714 and over the SEUS (asterisks).

715

716 Throughout the period of interest velocity-limited conditions are met at WOP (WFJ)
 717 with a frequency of $\sim 0.5\%$ ($\sim 2.5\%$) of the total time, reflecting again the sensitivity of droplet
 718 formation to aerosol fluctuations. During nighttime however, when lower σ_w values ($\sim 0.1 \text{ ms}^{-1}$)
 719 are recorded at WOP (Fig. 10c), we can observe some short periods characterized by
 720 intermediate to high N_{aer} ($> 1000 \text{ cm}^{-3}$) when the ratio N_d/N_d^{lim} exceeds ~ 0.65 , indicating that
 721 droplet variability is driven by updraft velocity. The σ_w values calculated at WFJ do not display
 722 a clear temporal pattern (Fig. 10d) but are generally higher than those recorded at the valley
 723 site. This is expected considering the steepness of the topography than can cause updraft
 724 velocities to be higher, especially for air-masses approaching the site from the north-easterly
 725 directions. Over the high mountain-top site cloud formation is in the velocity-limited regime
 726 (i.e., $N_d/N_d^{lim} > 0.65$) under high N_{aer} ($\sim 1500 \text{ cm}^{-3}$) and higher σ_w conditions ($\sim 0.8 \text{ ms}^{-1}$).

727 These conditions can be created when polluted air-masses from the valley site are vertically
 728 transported to WFJ.
 729



730
 731 **Figure 10.** Timeseries of potential N_d (cm^{-3}) (circles colored by N_{aer}) along with N_d^{lim} (cm^{-3})
 732 (black dashed line) and the ratio between those two (i.e., N_d/N_d^{lim}) (magenta dotted line),
 733 together with the timeseries of the calculated σ_w (ms^{-1}) (circles colored by N_{aer}), as estimated
 734 for WOP (a, c) and WFJ (b, d).

735

736 4. Summary and conclusions

737 The current study focuses on the aerosol-CCN-cloud droplet interplay in Alpine clouds
 738 sampled during the RACLETS field campaign over a two-week period of measurements
 739 conducted in the valley (WOP), and at the mountain-top station (WFJ). Our main objective was
 740 to investigate the drivers of droplet formation in MPCs formed in the region and understand in
 741 which situations N_d is sensitive to aerosol perturbations.

742 Overall, lower N_{aer} was systematically recorded at WFJ, indicating that the site is
 743 influenced by FT conditions. Deviations from this behavior are observed during fair weather
 744 conditions, when injections from the BL of lower altitudes can cause up to an order of
 745 magnitude elevation in the N_{aer} measured at WFJ. Combining the particle size distribution and
 746 CCN number concentration measured at WFJ, the average hygroscopicity parameter κ is about
 747 0.25, consistent with expectations for continental aerosol. The size-dependent κ reveals that
 748 accumulation mode particles are more hygroscopic than the smaller ones, which we attribute
 749 to an enrichment in organic material associated with primary emissions in the valley. The
 750 hygroscopicity of the particles at WFJ exhibit variations until February 28, which could reflect

751 BL injections from the valley. Precipitation events occurring between 1 and 8 March,
752 efficiently decrease N_{aer} , sometimes leaving some less hygroscopic particles.

753 Wind lidar products collected at WOP constrain the PDF of updraft velocities, which
754 combined with observed size distributions and hygroscopicity can be used to calculate the N_d
755 in clouds. We show predictions to agree within 25% with the limited observations of N_d
756 available. While this degree of closure has been achieved in past studies for liquid-phase
757 clouds, it has not been done at temperatures below freezing and with clouds containing ice –
758 as done here.

759 Combining the potential N_d and the corresponding S_{max} with the aerosol size distribution
760 data we sought to identify regimes where clouds formed are aerosol- or velocity-limited. We
761 found that when sufficient aerosol is present to decrease S_{max} below 0.1%, Alpine clouds
762 become velocity-limited, with the N_d reaching an upper limit, $N_d^{lim} \sim 150\text{-}550 \text{ cm}^{-3}$, that
763 depends on σ_w . Velocity-limited conditions occur when N_d/N_d^{lim} is above 0.65. Based on this
764 understanding, we deduce that droplet formation throughout the period of interest appears most
765 of the time to be aerosol-limited. More specifically, at the valley site, WOP, clouds become
766 sensitive to updraft velocity variations only during nighttime, when the BL turbulence is low.
767 Conversely, velocity-limited conditions are encountered at WFJ, during periods characterized
768 by elevated aerosol and CCN concentration levels ($>10^3 \text{ cm}^{-3}$) and higher σ_w values ($\sim 0.8 \text{ ms}^{-1}$).
769 Although variations in vertical velocity have not always been found to be the strongest factor
770 influencing the cloud microphysical characteristics, correct consideration of updraft velocity
771 fluctuations is crucial to fully understand the drivers of droplet variability and the role of
772 aerosol as a driver of N_d variability.

773 Interestingly, we find that the same linear relationship between N_d^{lim} and σ_w that
774 describes the droplet formation during RACLETS holds for warm boundary layer clouds
775 formed in the SE US (Bougiatioti et al., 2020) and in the SE Atlantic (Kacarab et al., 2019).
776 This implies that the $N_d^{lim} - \sigma_w$ relationship may be universal, given the wide range of cloud
777 formation conditions it represents. If so, measurements (or remote sensing) of N_d and vertical
778 velocity distribution alone may be used to determine if cloud droplet formation is susceptible
779 to aerosol variations or solely driven by vertical velocity – without any additional aerosol
780 information.

781 Approaching velocity-limited conditions also carries important implications for ice-
782 formation processes in MPCs – as high N_d means that droplet size and the probability of riming
783 becomes minimum. Indeed, Lance et al. (2011) saw that the concentration of large droplets

784 exceeding 30 μm diameter – critical for rime splintering or droplet shattering to occur – drops
785 considerably for polluted Arctic MPCs with LWC $\sim 0.2 \text{ gm}^{-3}$ and $N_d \sim 300\text{-}400 \text{ cm}^{-3}$. Assuming
786 that these levels of N_d reflects N_d^{lim} , the corresponding σ_w is 0.3-0.35 ms^{-1} (Fig. 9), which is
787 characteristic for Arctic stratus. The same phenomenon can also occur in the Alpine clouds
788 studied here, given that velocity-limited conditions ($N_d/N_d^{lim} > 0.65$) occurs especially during
789 nighttime (Fig. 10). Therefore, observations of N_d and vertical velocity distribution (i.e., N_d^{lim})
790 may possibly be used to determine if SIP from riming and droplet shattering is impeded, and
791 if occurring frequently enough may help explain the existence of persistent MPCs.

792

793 **Data Availability:** The data used in this study can be downloaded from the EnviDat data portal
794 at <https://www.envidat.ch/group/about/raclets-field-campaign>. The meteorological
795 measurements are provided by the Swiss Federal Office of Meteorology and Climatology
796 MeteoSwiss at <https://gate.meteoswiss.ch/idaweb/login.do>. The Gaussian fits used for
797 determining σ_w and the droplet parameterization used for the calculations in the study are
798 available from athanasios.nenes@epfl.ch upon request.

799

800 **Author Contributions:** PG and AN designed and initiated the study with methodology and
801 software developed by AN. The analysis was carried out by PG and AN, with input from ABo,
802 JW, CM, ZAK, JH, MH, ABe, UL. CCN instrumentation was setup by ABo, aerosol
803 instrumentation and inlet setup were done by JW, CM and ZAK, cloud data by FR, JH, lidar
804 data by MH. Instrument maintenance during the field campaign was carried out by JW and
805 CM. Data curation was provided by PG, AN, JW, CM, FR. The original manuscript was written
806 by PG and AN with input from all authors. All authors reviewed and commented on the
807 manuscript.

808

809 **Funding:** This study was supported by the European Research Council, CoG-2016 project
810 PyroTRACH (726165) funded by H2020-EU.1.1. – Excellent Science, and from the European
811 Union Horizon 2020 project FORCeS under grant agreement No 821205. JW, FR, ZAK, JH,
812 UL acknowledge funding from the Swiss National Science Foundation (SNSF) grant number
813 200021_175824. CM acknowledges funding from the SNSF grant number 200021_169620.

814

815 **Conflicts of Interest:** The authors declare no conflict of interest.

816 **References**

- 817 Andreae, M. O. and Rosenfeld, D.: Aerosol-cloud-precipitation interactions. Part 1. The nature
818 and sources of cloud-active aerosols, *Earth-Science Rev.*, 89, 13–41,
819 doi:10.1016/j.earscirev.2008.03.001, 2008.
- 820 Baltensperger, U., Gäggeler, H. W., Jost, D. T., Lugauer, M., Schwikowski, M., Weingartner,
821 E. and Seibert, P.: Aerosol climatology at the high-alpine site Jungfraujoch, Switzerland,
822 *J. Geophys. Res.*, 102, 1997.
- 823 Barahona, D., West, R. E. L., Stier, P., Romakkaniemi, S., Kokkola, H. and Nenes, A.:
824 Comprehensively accounting for the effect of giant CCN in cloud activation
825 parameterizations, *Atmos. Chem. Phys.*, 10, 2467–2473, doi:10.5194/acp-10-2467-2010,
826 2010.
- 827 Barahona, D., Molod, A., Bacmeister, J., Nenes, A., Gettelman, A., Morrison, H., Phillips, V.,
828 and Eichmann, A.: Development of two-moment cloud microphysics for liquid and ice
829 within the NASA Goddard Earth Observing System Model (GEOS-5), *Geosci. Model*
830 *Dev.*, 7, 1733–1766, doi:10.5194/gmd-7-1733-2014, 2014.
- 831 Beck, A., Henneberger, J., Schöpfer, S., Fugal, J. and Lohmann, U.: HoloGondel: In situ cloud
832 observations on a cable car in the Swiss Alps using a holographic imager, *Atmos. Meas.*
833 *Tech.*, 10, 459–476, doi:10.5194/amt-10-459-2017, 2017.
- 834 Bergeron, T.: On the physics of clouds and precipitation, Report, *Int. Union Geod. Geophys.*,
835 doi:10.1038/174957a0, 1935.
- 836 Borys, R. D., Lowenthal, D. H., Cohn, S. A. and Brown, W. O. J.: Mountaintop and radar
837 measurements of anthropogenic aerosol effects on snow growth and snowfall rate,
838 *Geophys. Res. Lett.*, 30, doi:10.1029/2002gl016855, 2003.
- 839 Bougiatioti, A., Bezantakos, S., Stavroulas, I., Kalivitis, N., Kokkalis, P., Biskos, G.,
840 Mihalopoulos, N., Papayannis, A. and Nenes, A.: Biomass-burning impact on CCN
841 number, hygroscopicity and cloud formation during summertime in the eastern
842 Mediterranean, *Atmos. Chem. Phys.*, 16, 7389–7409, doi:10.5194/acp-16-7389-2016,
843 2016.
- 844 Bougiatioti, A., Nenes, A., Lin, J., Brock, C., de Gouw, J., Liao, J., Middlebrook, A. and Welti,
845 A.: Drivers of cloud droplet number variability in the summertime Southeast United States,
846 *Atmos. Chem. Phys.*, 20, doi:10.5194/acp-20-12163-2020, 2020.
- 847 Chow, F. K., De Wekker, Stephan, F. J. and Snyder, B. J.: Mountain weather research and
848 forecasting: recent progress and current challenges., Dordrecht: Springer, 2013. Internet
849 resource.

850 Conant, W. C., VanReken, T. M., Rissman, T. A., Varutbangkul, V., Jonsson, H. H., Nenes,
851 A., Jimenez, J. L., Delia, A. E., Bahreini, R., Roberts, G. C., Flagan, R. C., and Seinfeld,
852 J. H.: Aerosol-cloud drop concentration closure in warm cumulus, *J. Geophys. Res.-*
853 *Atmos.*, 109, D13204, doi:10.1029/2003JD004324, 2004.

854 Dusek, U., Frank, G. P., Curtius, J., Drewnick, F., Schneider, J., Krten, A., Rose, D., Andreae,
855 M. O., Borrmann, S. and Pöschl, U.: Enhanced organic mass fraction and decreased
856 hygroscopicity of cloud condensation nuclei (CCN) during new particle formation events,
857 *Geophys. Res. Lett.*, 37, L03804, doi:10.1029/2009GL040930, 2010.

858 Fanourgakis, G. S., Kanakidou, M., Nenes, A., Bauer, S. E., Bergman, T., Carslaw, K. S., Grini,
859 A., Hamilton, D. S., Johnson, J. S., Karydis, V. A., Kirkevåg, A., Kodros, J. K., Lohmann,
860 U., Luo, G., Makkonen, R., Matsui, H., Neubauer, D., Pierce, J. R., Schmale, J., Stier, P.,
861 Tsigaridis, K., van Noije, T., Wang, H., Watson-Parris, D., Westervelt, D. M., Yang, Y.,
862 Yoshioka, M., Daskalakis, N., Decesari, S., Gysel Beer, M., Kalivitis, N., Liu, X.,
863 Mahowald, N. M., Myriokefalitakis, S., Schrödner, R., Sfakianaki, M., Tsimpidi, A. P.,
864 Wu, M. and Yu, F.: Evaluation of global simulations of aerosol particle number and cloud
865 condensation nuclei, and implications for cloud droplet formation, *Atmos. Chem. Phys.*
866 *Discuss.*, 19, 8591–8617, doi:10.5194/acp-19-8591-2019, 2019.

867 Farrington, R. J., Connolly, P. J., Lloyd, G., Bower, K. N., Flynn, M. J., Gallagher, M. W.,
868 Field, P. R., Dearden, C. and Choulaton, T. W.: Comparing model and measured ice
869 crystal concentrations in orographic clouds during the INUPIAQ campaign, *Atmos. Chem.*
870 *Phys.*, 16, 4945–4966, doi:10.5194/acp-16-4945-2016, 2016.

871 Field, P. R., Lawson, R. P., Brown, P. R. A., Lloyd, G., Westbrook, C., Moisseev, D.,
872 Miltenberger, A., Nenes, A., Blyth, A., Choulaton, T., Connolly, P., Buehl, J., Crosier, J.,
873 Cui, Z., Dearden, C., DeMott, P., Flossmann, A., Heymsfield, A., Huang, Y., Kalesse, H.,
874 Kanji, Z. A., Korolev, A., Kirchgaessner, A., Lasher-Trapp, S., Leisner, T., McFarquhar,
875 G., Phillips, V., Stith, J. and Sullivan, S.: Chapter 7. Secondary Ice Production - current
876 state of the science and recommendations for the future, *Meteorol. Monogr.*,
877 doi:10.1175/amsmonographs-d-16-0014.1, 2017.

878 Findeisen, W.: Die kolloidmeteorologischen vorgänge bei der niederschlagsbildung, *Meteorol.*
879 *Zeitschrift*, 55, 121–133, 1938.

880 Fountoukis, C. and Nenes, A.: Continued development of a cloud droplet formation
881 parameterization for global climate models, *J. Geophys. Res.*, 110, D1121,
882 doi:10.1029/2004JD005591, 2005.

883 Fountoukis, C., Nenes, A., Meskhidze, N., Bahreini, R., Conant, W. C., Jonsson, H., Murphy,

884 S., Sorooshian, A., Varutbangkul, V., Brechtel, F., Flagan, R. C. and Seinfeld, J. H.:
885 Aerosol-cloud drop concentration closure for clouds sampled during the International
886 Consortium for Atmospheric Research on Transport and Transformation 2004 campaign,
887 *J. Geophys. Res.*, 112, doi:10.1029/2006JD007272, 2007.

888 Fugal, J. P., Schulz, T. J. and Shaw, R. A.: Practical methods for automated reconstruction and
889 characterization of particles in digital in-line holograms, *Meas. Sci. Technol.*, 20,
890 doi:10.1088/0957-0233/20/7/075501, 2009.

891 Ghan, S., Guzman, G., and Abdul-Razzak, H.: Competition between sea salt and sulfate
892 particles as cloud condensation nuclei, *J. Atmos. Sci.*, 55, 3340–3347, 1998.

893 Ghan, S.J., Abdul-Razzak, H., Nenes, A., Ming, Y., Liu, X., Ovchinnikov, M., Shipway, B.,
894 Meskhidze, N., Xu, J. and Shi, X.: Droplet Nucleation: Physically-based Parameterization
895 and Comparative Evaluation, *J. Adv. Model. Earth Syst.*, 3, doi:10.1029/2011MS000074,
896 2011.

897 Griesche, H. J., Seifert, P., Ansmann, A., Baars, H., Barrientos Velasco, C., Bühl, J.,
898 Engelmann, R., Radenz, M. and Zhenping, Y.: Application of the shipborne remote
899 sensing supersite OCEANET for profiling of Arctic aerosols and clouds during Polarstern
900 cruise PS106, *Atmos. Meas. Tech. Discuss.*, 1–37, doi:10.5194/amt-2019-434, 2019.

901 Grosvenor, D. P., Sourdeval, O., Zuidema, P., Ackerman, A., Alexandrov, M. D., Bennartz,
902 R., Boers, R., Cairns, B., Chiu, J. C., Christensen, M., Deneke, H., Diamond, M., Feingold,
903 G., Fridlind, A., Hünerbein, A., Knist, C., Kollias, P., Marshak, A., McCoy, D., Merk, D.,
904 Painemal, D., Rausch, J., Rosenfeld, J., Russchenberg, H., Seifert, P., Sinclair, K., Stier,
905 P., van Diedenhoven, B., Wendisch, M., Werner, F., Wood, R., Zhang, Z. and Quaas, J.:
906 Remote sensing of droplet number concentration in warm clouds: A review of the current
907 state of knowledge and perspectives. *Reviews of Geophysics*, 56, 409–453.
908 doi:10.1029/2017RG000593, 2018.

909 Grubisic, V. and Billings, B. J.: Climatology of the Sierra Nevada mountain-wave events, *Mon.*
910 *Weather Rev.*, 136, 757–768, doi:10.1175/2007MWR1902.1, 2008.

911 Hammer, E., Bukowiecki, N., Gysel, M., Jurányi, Z., Hoyle, C. R., Vogt, R., Baltensperger, U.
912 and Weingartner, E.: Investigation of the effective peak supersaturation for liquid-phase
913 clouds at the high-alpine site Jungfraujoch, Switzerland (3580 m a.s.l.), *Atmos. Chem.*
914 *Phys.*, 14, 1123–1139, doi:10.5194/acp-14-1123-2014, 2014.

915 Hammer, E., Bukowiecki, N., Luo, B. P., Lohmann, U., Marcolli, C., Weingartner, E.,
916 Baltensperger, U. and Hoyle, C. R.: Sensitivity estimations for cloud droplet formation in
917 the vicinity of the high-alpine research station Jungfraujoch (3580 m a.s.l.), *Atmos. Chem.*

918 Phys., 15, 10309–10323, doi:10.5194/acp-15-10309-2015, 2015.

919 Henneberg, O., Henneberger, J. and Lohmann, U.: Formation and development of orographic
920 mixed-phase clouds, *J. Atmos. Sci.*, 74, 3703–3724, doi:10.1175/JAS-D-16-0348.1, 2017.

921 Henneberger, J., Fugal, J. P., Stetzer, O. and Lohmann, U.: HOLIMO II: A digital holographic
922 instrument for ground-based in situ observations of microphysical properties of mixed-
923 phase clouds, *Atmos. Meas. Tech.*, 6, 2975–2987, doi:10.5194/amt-6-2975-2013, 2013.

924 Herrmann, E., Weingartner, E., Henne, S., Vuilleumier, L., Bukowiecki, N., Steinbacher, M.,
925 Conen, F., Collaud Coen, M., Hammer, E., Jurányi, Z., Baltensperger, U. and Gysel, M.:
926 Analysis of long-term aerosol size distribution data from Jungfraujoch with emphasis on
927 free tropospheric conditions, cloud influence, and air mass transport, *J. Geophys. Res.*
928 *Atmos.*, 120, 9459–9480, doi:10.1002/2015JD023660, 2015.

929 Hoyle, C. R., Webster, C. S., Rieder, H. E., Nenes, A., Hammer, E., Herrmann, E., Gysel, M.,
930 Bukowiecki, N., Weingartner, E., Steinbacher, M. and Baltensperger, U.: Chemical and
931 physical influences on aerosol activation in liquid clouds : a study based on observations
932 from the Jungfraujoch , Switzerland, *Atmos. Chem. Phys.*, 16, 4043–4061,
933 doi:10.5194/acp-16-4043-2016, 2016.

934 IPCC: Climate Change 2013: The Physical Science Basis. Contribution of Working Group I to
935 the Fifth Assessment Report of the Intergovernmental Panel on Climate Change, edited
936 by: Stocker, T. F., Qin, D., Plattner, G.-K., Tignor, M., Allen, S. K., Boschung, Cambridge
937 Univ. Press. Cambridge, UK New York, NY, USA, 1535 pp.,
938 doi:10.1017/CBO9781107415324, 2013.

939 Jensen, J. B. and Charlson R. J.: On the efficiency of nucleation scavenging, *Tellus*, 36B, 367–
940 375, doi: 10.3402/tellusb.v36i5.14917, 1984.

941 Jurányi, Z., Gysel, M., Weingartner, E., Decarlo, P. F., Kammermann, L. and Baltensperger,
942 U.: Measured and modelled cloud condensation nuclei number concentration at the high
943 alpine site Jungfraujoch, *Atmos. Chem. Phys.*, 10, 7891–7906, doi:10.5194/acp-10-7891-
944 2010, 2010.

945 Jurányi, Z., Gysel, M., Weingartner, E., Bukowiecki, N., Kammermann, L. and Baltensperger,
946 U.: A 17 month climatology of the cloud condensation nuclei number concentration at the
947 high alpine site Jungfraujoch, *J. Geophys. Res.*, 116, D1020, doi:10.1029/2010JD015199,
948 2011.

949 Kacarab, M., Lee Thornhill, K., Dobracki, A., Howell, S. G., O’Brien, J. R., Freitag, S., Poellot,
950 M. R., Wood, R., Zuidema, P., Redemann, J. and Nenes, A.: Biomass burning aerosol as
951 a modulator of the droplet number in the southeast Atlantic region, *Atmos. Chem. Phys.*,

952 20, 3029–3040, doi:10.5194/acp-20-3029-2020, 2020.

953 Kalkavouras, P., Bougiatioti, A., Kalivitis, N., Stavroulas, I., Tombrou, M., Nenes, A. and
954 Mihalopoulos, N.: Regional new particle formation as modulators of cloud condensation
955 nuclei and cloud droplet number in the eastern Mediterranean, *Atmos. Chem. Phys.*, 19,
956 6185–6203, doi:10.5194/acp-19-6185-2019, 2019.

957 Kammermann, L., Gysel, M., Weingartner, E. and Baltensperger, U.: 13-month climatology of
958 the aerosol hygroscopicity at the free tropospheric site Jungfraujoch (3580 m a.s.l.),
959 *Atmos. Chem. Phys.*, 10, doi:10.5194/acp-10-10717-2010, 2010.

960 Kleissl, J., Honrath, R. E., Dziobak, M. P., Tanner, D., Val Martín, M., Owen, R. C. and
961 Helmig, D.: Occurrence of upslope flows at the Pico mountaintop observatory: A case
962 study of orographic flows on a small, volcanic island, *J. Geophys. Res. Atmos.*, 112,
963 D10S3, doi:10.1029/2006JD007565, 2007.

964 Korolev, A. and Isaac, G.: Phase transformation of mixed-phase clouds, *Q. J. R. Meteorol.*
965 *Soc.*, 129, 19–38, doi:10.1256/qj.01.203, 2003.

966 Lance, S., Shupe, M. D., Feingold, G., Brock, C. A., Cozic, J., Holloway, J. S., Moore, R. H.,
967 Nenes, A., Schwarz, J. P., Spackman, J. R., Froyd, K. D., Murphy, D. M., Brioude, J.,
968 Cooper, O. R., Stohl, A. and Burkhardt, J. F.: Cloud condensation nuclei as a modulator of
969 ice processes in Arctic mixed-phase clouds, *Atmos. Chem. Phys.*, 11, 8003–8015,
970 doi:10.5194/acp-11-8003-2011, 2011.

971 Lanz, V. A., Prévôt, A. S. H., Alfarra, M. R., Weimer, S., Mohr, C., Decarlo, P. F., Gianini, M.
972 F. D., Hueglin, C., Schneider, J., Favez, O., D’Anna, B., George, C. and Baltensperger,
973 U.: Characterization of aerosol chemical composition with aerosol mass spectrometry in
974 Central Europe: An overview, *Atmos. Chem. Phys.*, 10, 10453–10471, doi:10.5194/acp-
975 10-10453-2010, 2010.

976 Latham, T. L., Beyersdorf, A. J., Thornhill, K. L., Winstead, E. L., Cubison, M. J., Hecobian,
977 A., Jimenez, J. L., Weber, R. J., Anderson, B. E. and Nenes, A.: Analysis of CCN activity
978 of Arctic aerosol and Canadian biomass burning during summer 2008, *Atmos. Chem.*
979 *Phys.*, 13, 2735–2756, doi:10.5194/acp-13-2735-2013, 2013.

980 Lauber, A., Henneberger, J., Mignani, C., Ramelli, F., Pasquier, J. T., Wieder, J., Hervo, M.,
981 and Lohmann, U.: Continuous secondary-ice production initiated by updrafts through the
982 melting layer in mountainous regions, *Atmos. Chem. Phys.*, 21, 3855–3870,
983 doi:10.5194/acp-21-3855-2021, 2021.

984 Lloyd, G., Choulaton, T. W., Bower, K. N., Gallagher, M. W., Connolly, P. J., Flynn, M.,
985 Farrington, R., Crosier, J., Schlenczek, O., Fugal, J. and Henneberger, J.: The origins of

986 ice crystals measured in mixed-phase clouds at the high-alpine site Jungfraujoch, *Atmos.*
987 *Chem. Phys.*, 15, 12953–12969, doi:10.5194/acp-15-12953-2015, 2015.

988 Lohmann, U.: A glaciation indirect aerosol effect caused by soot aerosols, *Geophys. Res. Lett.*,
989 29(4), doi:10.1029/2001GL014357, 2002.

990 Lohmann, U. and Feichter, J.: Global indirect aerosol effects: a review, *Atmos. Chem. Phys.*,
991 5, 715–737, doi:10.5194/acp-5-715-2005, 2005.

992 Lohmann, U., Henneberger, J., Henneberg, O., Fugal, J. P., Bühl, J. and Kanji, Z. A.:
993 Persistence of orographic mixed-phase clouds, *Geophys. Res. Lett.*, 43, 10512–10519,
994 doi:10.1002/2016GL071036, 2016.

995 Lohmann, U.: Anthropogenic Aerosol Influences on Mixed-Phase Clouds, *Curr. Clim. Chang.*
996 *Reports*, 3, 32–44, doi:10.1007/s40641-017-0059-9, 2017.

997 Meskhidze, N., Nenes, A., Conant, W. C. and Seinfeld, J. H.: Evaluation of a new cloud droplet
998 activation parameterization with in situ data from CRYSTAL-FACE and CSTRIFE, *J.*
999 *Geophys. Res.*, 110, D1620, doi:10.1029/2004JD005703, 2005.

1000 Mignani, C., Creamean, J. M., Zimmermann, L., Alewell, C., and Conen, F.: New type of
1001 evidence for secondary ice formation at around -15°C in mixed-phase clouds, *Atmos.*
1002 *Chem. Phys.*, 19, 877–886, doi:10.5194/acp-19-877-2019, 2019.

1003 Mignani, C., Wieder, J., Sprenger, M. A., Kanji, Z. A., Henneberger, J., Alewell, C. and Conen,
1004 F.: Towards parameterising atmospheric concentrations of ice-nucleating particles active
1005 at moderate supercooling, *Atmos. Chem. Phys.*, 21, 657–664, doi:10.5194/acp-21-657-
1006 2021, 2021.

1007 Moore, R. H., Bahreini, R., Brock, C. A., Froyd, K. D., Cozic, J., Holloway, J. S., Middlebrook,
1008 A. M., Murphy, D. M. and Nenes, A.: Hygroscopicity and composition of Alaskan Arctic
1009 CCN during April 2008, *Atmos. Chem. Phys.*, 11, 11807–11825, doi:10.5194/acp-11-
1010 11807-2011, 2011.

1011 Morales Betancourt, R. and Nenes, A.: Characteristic updrafts for computing distribution-
1012 averaged cloud droplet number and stratocumulus cloud properties, *J. Geophys. Res.*, 115,
1013 D1822, doi:10.1029/2009JD013233, 2010.

1014 Morales Betancourt, R., Nenes, A., Jonsson, H., Flagan, R. C. and Seinfeld, J. H.: Evaluation
1015 of an entraining droplet activation parameterization using in situ cloud data, *J. Geophys.*
1016 *Res.*, 116, D1520, doi:10.1029/2010JD015324, 2011.

1017 Morales Betancourt, R., and Nenes, A.: Aerosol Activation Parameterization: The population
1018 splitting concept revisited, *Geosci.Mod.Dev.*, 7, 2345–2357, doi:10.5194/gmd-7-2345-
1019 2014, 2014.

1020 Mosimann, L, Weingartner, E. and Waldvogel A.: An analysis of accreted drop sizes and mass
1021 on rimed snow crystals., *J. Atmos. Sci.*, 51, 1548–1558, 1994.

1022 Muhlbauer, A. and Lohmann, U.: Sensitivity studies of aerosol-cloud interactions in mixed-
1023 phase orographic precipitation, *J. Atmos. Sci.*, 66, 2517–2538,
1024 doi:10.1175/2009JAS3001.1, 2009.

1025 Nenes., A., Ghan, S., Abdul-Razzak, H., Chuang, P.Y., Seinfeld, J.H.: Kinetic Limitations on
1026 Cloud Droplet Formation and Impact on Cloud Albedo, *Tellus*, 53B, 133-149, 2001.

1027 Nenes, A. and Seinfeld, J. H.: Parameterization of cloud droplet formation in global climate
1028 models, *J. Geophys. Res.*, 108, 4415, doi:10.1029/2002jd002911, 2003.

1029 Okamoto, S. and Tanimoto, H.: A review of atmospheric chemistry observations at mountain
1030 sites, *Prog. Earth Planet. Sci.*, 3, 34, doi:10.1186/s40645-016-0109-2, 2016.

1031 Petters, M. D. and Kreidenweis, S. M.: A single parameter representation of hygroscopic
1032 growth and cloud condensation nucleus activity, *Atmos. Chem. Phys.*, 7, 1961–1971,
1033 doi:10.5194/acp-7-1961-2007, 2007.

1034 Pringle, K. J., Tost, H., Pozzer, A., Pöschl, U. and Lelieveld, J.: Global distribution of the
1035 effective aerosol hygroscopicity parameter for CCN activation, *Atmos. Chem. Phys.*, 10,
1036 5241–5255, doi:10.5194/acp-10-5241-2010, 2010.

1037 Pruppacher, H. R. and Klett, J. D.: *Microphysics of Clouds and Precipitation*, 2nd ed., 1997.

1038 Ramelli, F., Beck, A., Henneberger, J. and Lohmann, U.: Using a holographic imager on a
1039 tethered balloon system for microphysical observations of boundary layer clouds, *Atmos.*
1040 *Meas. Tech.*, 13, 925–939, doi:10.5194/amt-13-925-2020, 2020.

1041 Ramelli, F., Henneberger, J., David, R. O., Lauber, A., Pasquier, J. T., Wieder, J., Bühl, J.,
1042 Seifert, P., Engelmann, R., Hervo, M., and Lohmann, U.: Influence of low-level blocking
1043 and turbulence on the microphysics of a mixed-phase cloud in an inner-Alpine valley,
1044 *Atmos. Chem. Phys.*, 21, 5151–5172, doi:10.5194/acp-21-5151-2021, 2021a.

1045 Ramelli, F., Henneberger, J., David, R. O., Bühl, J., Radenz, M., Seifert, P., Wieder, J., Lauber,
1046 A., Pasquier, J. T., Engelmann, R., Mignani, C., Hervo, M., and Lohmann, U.:
1047 Microphysical investigation of the seeder and feeder region of an Alpine mixed-phase
1048 cloud, *Atmos. Chem. Phys.*, 21, 6681–6706, doi:10.5194/acp-21-6681-2021, 2021b.

1049 Reutter, P., Su, H., Trentmann, J., Simmel, M., Rose, D., Gunthe, S. S., Wernli, H., Andreae,
1050 M. O. and Pöschl, U.: Aerosol- and updraft-limited regimes of cloud droplet formation:
1051 Influence of particle number, size and hygroscopicity on the activation of cloud
1052 condensation nuclei (CCN), *Atmos. Chem. Phys.*, 9, 7067–7080, doi:10.5194/acp-9-7067-
1053 2009, 2009.

1054 Roberts, G. C. and Nenes, A.: A continuous-flow streamwise thermal-gradient CCN chamber
1055 for atmospheric measurements, *Aerosol Sci. Technol.*, 39(3), 206–221,
1056 doi:10.1080/027868290913988, 2005.

1057 Roe, G. H.: Orographic Precipitation, *Annu. Rev. Earth Planet. Sci.*, 33, 645–671,
1058 doi:10.1146/annurev.earth.33.092203.122541, 2005.

1059 Rose, D., Gunthe, S. S., Mikhailov, E., Frank, G. P., Dusek, U., Andreae, M. O. and Pöschl,
1060 U.: Calibration and measurement uncertainties of a continuous-flow cloud condensation
1061 nuclei counter (DMT-CCNC): CCN activation of ammonium sulfate and sodium chloride
1062 aerosol particles in theory and experiment, *Atmos. Chem. Phys.*, 8(5), 1153–1179,
1063 doi:10.5194/acp-8-1153-2008, 2008.

1064 Rotunno, R. and Houze, R. A.: Lessons on orographic precipitation from the Mesoscale Alpine
1065 Programme, *Q. J. R. Meteorol. Soc.*, 133, 811–830, doi:10.1002/qj.67, 2007.

1066 Saleeby, S. M., Cotton, W. R., Lowenthal, D. and Messina, J.: Aerosol impacts on the
1067 microphysical growth processes of orographic snowfall, *J. Appl. Meteorol. Climatol.*, 52,
1068 834–852, doi:10.1175/JAMC-D-12-0193.1, 2013.

1069 Seinfeld, J. H. and Pandis, S. N.: *Atmospheric Chemistry and Physics: From Air Pollution to*
1070 *Climate Change*, 2nd Edn., John Wiley, edited by: Hoboken, N. J., 2006.

1071 Seinfeld, J. H., Bretherton, C., Carslaw, K. S., Coe, H., DeMott, P. J., Dunlea, E. J., Feingold,
1072 G., Ghan, S., Guenther, A. B., Kahn, R., Kraucunas, I., Kreidenweis, S. M., Molina, M. J.,
1073 Nenes, A., Penner, J. E., Prather, K. A., Ramanathan, V., Ramaswamy, V., Rasch, P. J.,
1074 Ravishankara, A. R., Rosenfeld, D., Stephens, G. and Wood, R.: Improving our
1075 fundamental understanding of the role of aerosol-cloud interactions in the climate system,
1076 *Proc. Natl. Acad. Sci. U. S. A.*, 113, 5781–5790, doi:10.1073/pnas.1514043113, 2016.

1077 Smith, R. B.: Progress on the theory of orographic precipitation, *Spec. Pap. Geol. Soc. Am.*,
1078 398, 1–16, doi:10.1130/2006.2398(01), 2006.

1079 Snider, J. R., Leon, D. and Wang, Z.: Droplet concentration and spectral broadening in
1080 Southeast Pacific stratocumulus clouds, *J. Atmos. Sci.*, 74(3), 719–749. doi:10.1175/JAS-
1081 D-16-0043.1, 2017.

1082 Sotiropoulou, G., Sullivan, S., Savre, J., Lloyd, G., Lachlan-Cope, T., Ekman, A. M. L. and
1083 Nenes, A.: The impact of secondary ice production on Arctic stratocumulus, *Atmos. Chem.*
1084 *Phys.*, 20, 1301–1316, doi:10.5194/acp-20-1301-2020, 2020.

1085 Sotiropoulou, G., Vignon, É., Young, G., Morrison, H., O'Shea, S. J., Lachlan-Cope, T., Berne,
1086 A., and Nenes, A.: Secondary ice production in summer clouds over the Antarctic coast:
1087 an underappreciated process in atmospheric models, *Atmos. Chem. Phys.*, 21, 755–771,

1088 <https://doi.org/10.5194/acp-21-755-2021>, 2021.

1089 Sud, Y.C, Lee, D., Oreopoulos, L., Barahona, D., Nenes, A. and M.J. Suarez: Performance of
1090 McRAS-AC in the GEOS-5 AGCM: aerosol-cloud-microphysics, precipitation, cloud
1091 radiative effects, and circulation, *Geosci. Model. Dev.*, 6, 57–79, doi:10.5194/gmd-6-57-
1092 2013, 2013.

1093 Sullivan, S. C., Lee, D., Oreopoulos, L. and Nenes, A.: Role of updraft velocity in temporal
1094 variability of global cloud hydrometeor number, *Proc. Natl. Acad. Sci. U. S. A.*, 113,
1095 5791–5796, doi:10.1073/pnas.1514039113, 2016.

1096 Sullivan, S. C., Barthlott, C., Crosier, J., Zhukov, I., Nenes, A. and Hoose, C.: The effect of
1097 secondary ice production parameterization on the simulation of a cold frontal rainband,
1098 *Atmos. Chem. Phys.*, 18, 16461–16480, doi:10.5194/acp-18-16461-2018, 2018.

1099 Tokay, A., Wolff, D. B. and Petersen, W. A.: Evaluation of the new version of the laser-optical
1100 disdrometer, OTT parsivel, *J. Atmos. Ocean. Technol.*, 31(6), 1276–1288,
1101 doi:10.1175/JTECH-D-13-00174.1, 2014.

1102 Touloupas, G., Lauber, A., Henneberger, J., Beck, A. and Lucchi, A.: A convolutional neural
1103 network for classifying cloud particles recorded by imaging probes, *Atmos. Meas. Tech.*,
1104 13(5), 2219–2239, doi:10.5194/amt-13-2219-2020, 2020.

1105 Tröstl, J., Herrmann, E., Frege, C., Bianchi, F., Molteni, U., Bukowiecki, N., Hoyle, C. R.,
1106 Steinbacher, M., Weingartner, E., Dommen, J., Gysel, M. and Baltensperger, U.:
1107 Contribution of new particle formation to the total aerosol concentration at the high-
1108 altitude site Jungfraujoch (3580masl, Switzerland), *J. Geophys. Res. Atmos.*, 121, 11692–
1109 11711, doi:10.1002/2015JD024637, 2016.

1110 Twomey, S., Radiative properties of clouds, pp. 278 – 280, in *Aerosol Effects on Climate*, S.G.
1111 Jennings Editor, The University of Arizona Press, Tucson, 1993.

1112 Vosper, S. B., Wells, H., Sinclair, J. A. and Sheridan, P. F.: A climatology of lee waves over
1113 the UK derived from model forecasts, *Meteorol. Appl.*, 20, 466–481,
1114 doi:10.1002/met.1311, 2013.

1115 Wang, J., Lee, Y. N., Daum, P. H., Jayne, J. and Alexander, M. L.: Effects of aerosol organics
1116 on cloud condensation nucleus (CCN) concentration and first indirect aerosol effect,
1117 *Atmos. Chem. Phys.*, 8, 6325–6339, doi:10.5194/acp-8-6325-2008, 2008.

1118 Wegener, A.: *Thermodynamik der Atmosphäre*, Ger. Barth, Leipzig, 331 pp., 1911.

1119 Zubler, E. M., Lohmann, U., Lüthi, D., Schär, C. and Muhlbauer, A.: Statistical analysis of
1120 aerosol effects on simulated mixed-phase clouds and precipitation in the Alps, *J. Atmos.*
1121 *Sci.*, 68, 1474–1492, doi:10.1175/2011JAS3632.1, 2011.